NASA HyTEC CMC Turbine Blade Durability

Dane Dale, Alex Ruschau

GE Aerospace, Cincinnati, Ohio

Prepared under Contract NNC15BA05B / 80GRC020F0081

Contents

Section Page

Figures

Tables

1.0 Summary

The objective of the CMC turbine blade durability program is to identify critical material and design parameters that affect durability of ceramic matrix composite (CMC) turbine blades. A baseline architecture for a cooled high-pressure turbine (HPT) CMC blade and accompanying sub-component test articles were developed with the intent to demonstrate through analysis and subcomponent testing how material and design parameters impact key failure modes.

As part of this program, a notional architecture for a cooled CMC blade was matured through a design review rhythm to produce a blade test article containing the necessary features required for operation in an engine like environment. Further validation of the durability of these features were achieved through coupon and sub-component testing to demonstrate the durability of cooling hole configurations and blade attachment designs.

Analytical methods were also used to evaluate the acceptability of the baseline blade test article architecture against relevant design requirements and identify abatement and recommended changes to key design drivers to improve component durability for future design iterations.

2.0 Introduction

To achieve these objectives GE Aerospace is leveraging its experience and significant investment in the development of its CMC material system. These developments led to the commercial introduction of high-pressure turbine shrouds in the LEAP engine and the incorporation of multiple CMC hot section components in the GE9X engine, including inner and outer combustor liners, HPT Stage 1 Nozzles, HPT Stage 1 Shrouds, and HPT Stage 2 nozzles. Directly relevant to the development of a CMC high pressure turbine blade, GE has extensive experience with cooled static turbine airfoils in addition to experience with uncooled CMC turbine blades located in the low-pressure turbine.

3.0 Task 1 – Test Article Design

3.1 Objective

The objective of Task 1 is to identify a representative baseline design for a cooled CMC high pressure turbine blade test article. This test article incorporates all of the relevant features for operation at engine relevant conditions including: cooling circuit and temperature capability, disk attachment, leading and trailing edges, and an environmental barrier coating. A structured design process was implemented to mature a blade test article design from the conceptual design phase through an initial configuration assessment against engine relevant conditions. Design efforts included aerodynamic, mechanical, and thermal design of a representative blade test article.

3.2 Design Space Selection

There are multiple engine applications, such as long-haul commercial turbofans (i.e., GE90 engine, GEnx engine), short haul commercial turbofans (i.e., CFM56 engine, LEAP engine) and military low bypass turbofans (i.e., F101 engine, F110 engine), that provide unique combinations of design parameters such as mechanical loading, thermal environment, and geometric scale.

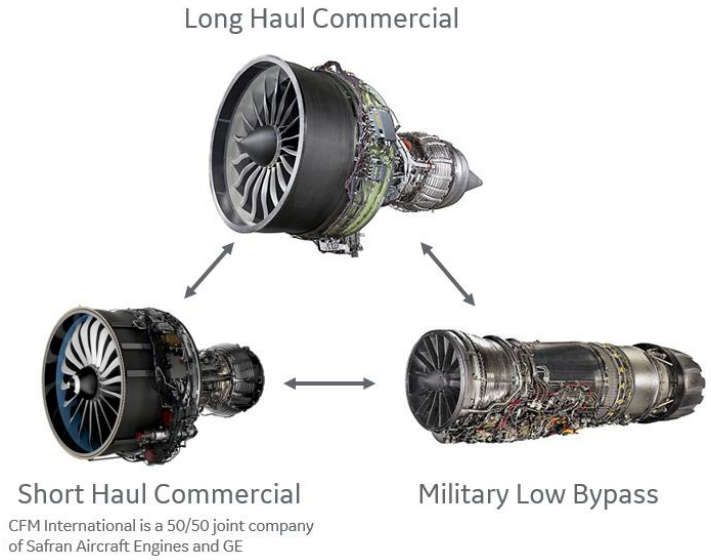

Figure 3.001 – Depiction of variation in engine architecture

Relative to the objectives of the CMC turbine blade durability program, all aforementioned engine architectures and configurations provide a suitable platform for assessment. However, due to the low technical maturity and manufacturing readiness for cooled ceramic matrix composite turbine blades, consideration was given to the application that would serve as the basis for the development of the baseline cooled CMC blade configuration. The geometric scale of the test article was a key design parameter of interest for this program with several attributes considered:

- Component volume available providing flexibility in selection and implementation of cooling concepts and geometries
- Component scale relative to the feature size capability of current low-volume manufacturing techniques and processes, and consideration for test article yield
- Physical size providing feature size range of design parameters

With these attributes in consideration, it was desirable to base the design approach on a larger, long haul commercial turbofan consideration. Germane to this study, the configuration chosen was the GEnx engine, a long-haul commercial turbofan in the 70,000 lbf thrust class. This platform provides adequate size required for early manufacturing readiness level (MRL) manufacturing techniques while also being a technically relevant, modern engine. The general design space of the high-pressure turbine blade is shown below in Table 3.001 and Figure 3.002.

Table 3.001: Blade design space parameters

Parameter	Lower Bound	Upper Bound
Airfoil Height (H_A)	2.0”	2.1”
Blade Height (H_B)	3.4”	3.8”
Dovetail Length (L_D)	1.4”	1.7”
Chord Length (C)	1.3”	1.5”
Axial Width (AW)	1.0”	1.3”

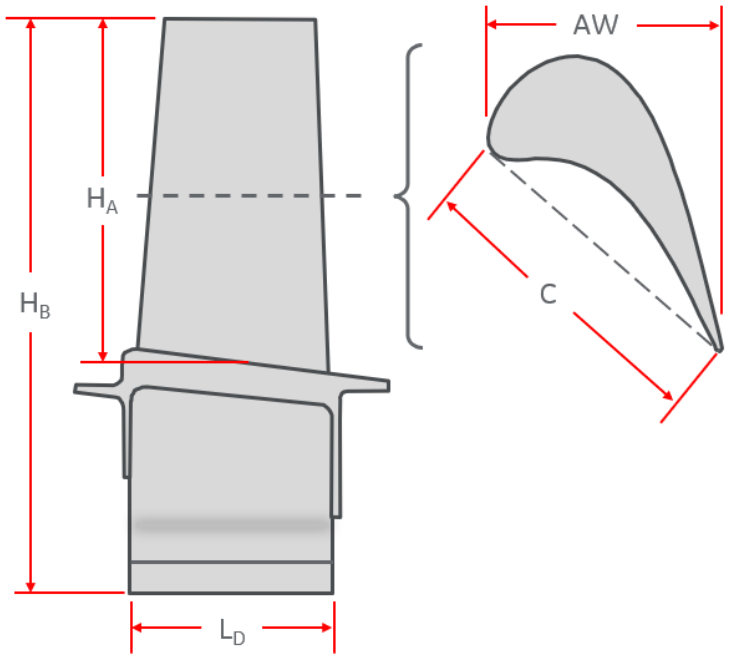

Figure 3.002 - Blade configuration overview

3.3 Baseline Blade Test Article Mechanical Design

The following sections will cover the design process of establishing the baseline design of the blade test article. Figure 3.003 provides the high-pressure turbine blade nomenclature to be discussed throughout this report.

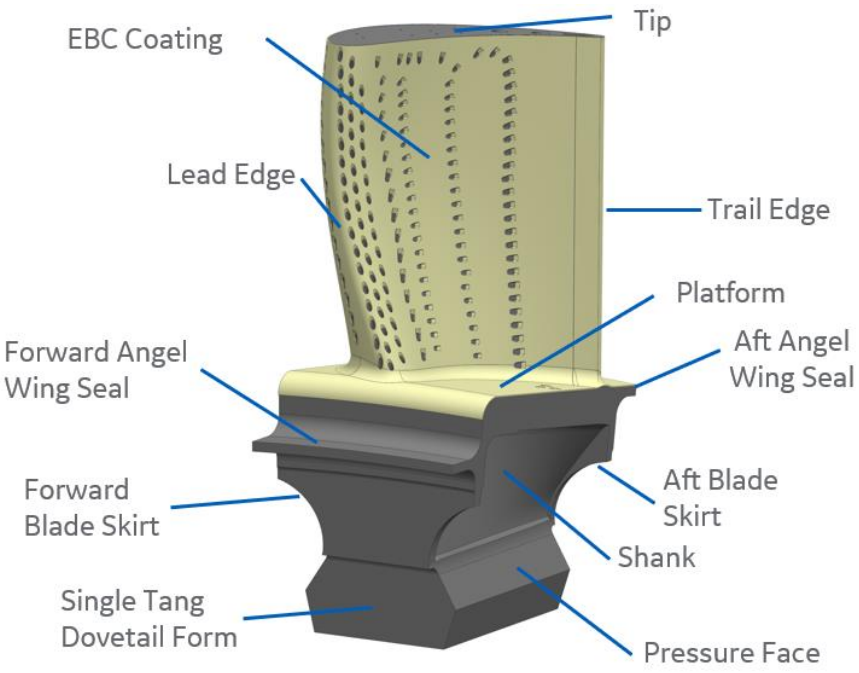

Figure 3.003 - Blade test article overview and nomenclature

3.3.1 Airfoil Design

The basis for the airfoil design of the baseline CMC cooled blade will be pulled from the configurations of metallic blades on existing GE engines, with modifications made to adapt design features to improve compatibility with a composite lay-up process. The baseline CMC test article airfoil targeted the same performance and aerodynamic characteristics of those metallic blades, with additional consideration given to the manufacturing needs and material capability of the CMC material.

The most important consideration for the design of the airfoil is the incorporation of the cooling architectures. Typical metallic turbine blades have complex cooling circuits forming serpentine passages, or even a plurality of cooling circuits. It is also common for metallic high pressure turbine blades to incorporate features within the cooling circuits that increase the heat transfer coefficient locally allowing for more efficient internal cooling designs not reliant upon film cooling on the outer surface. These features are difficult to incorporate into a composite component that is manufactured through a composite lay-up process where internal tooling would have to be removed from the part. It is also a challenge to incorporate complex cooling circuit designs (such as serpentine passages) as it is desirable for the airfoil of a CMC blade to contain continuous fiber for durability. With these constraints, simpler cooling configurations such as radially oriented passages are preferred.

Figure 3.004 details two radially oriented cooling passage configurations that were considered for the CMC blade test article. A concept airfoil, representative of a high-pressure turbine blade

airfoil, was used for cavity lay-out and generation of a finite element model for pressure only evaluation.

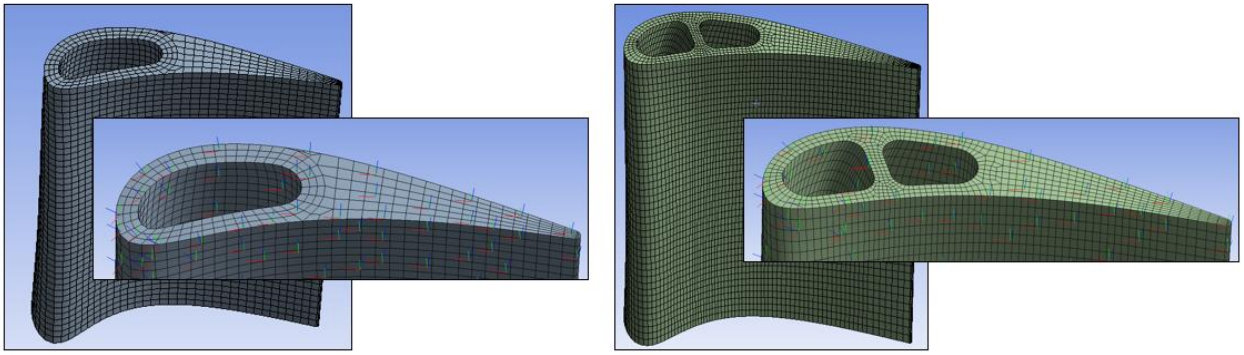

(a) (b)

Figure 3.004: Finite element models of (a) a single cavity airfoil and (b) a double cavity airfoil with rib

A key concern relative to the cavity configuration is the ability to contain the internal pressure of the cooling air. A large single cavity, while simpler to construct, will have a larger internal surface area and will therefore exhibit higher ballooning stresses oriented in the hoop direction around the cavity. A multi-cavity configuration allows for small cavities, to reduce the pressure loading, but mechanically links the pressure and suction sides of the airfoil through the rib. This mechanical linkage may become a design challenge when thermal gradients are introduced through the flowpath walls and rib of the airfoil.

The airfoil configurations were screened using mechanical-only pressure loading using an engine relevant internal pressure differential of 342 psi for the single cavity airfoil and differential pressures of 342 psi (forward cavity) and 250 psi (aft cavity) for the double cavity airfoil. The airfoil only models also contain an element coordinate system alignment to apply directionally dependent material properties. Both models have element co-ordinate systems aligned relative to the mean camber surface of the airfoil. Stress contours are plotted with the section views shown below in Figure 3.005.

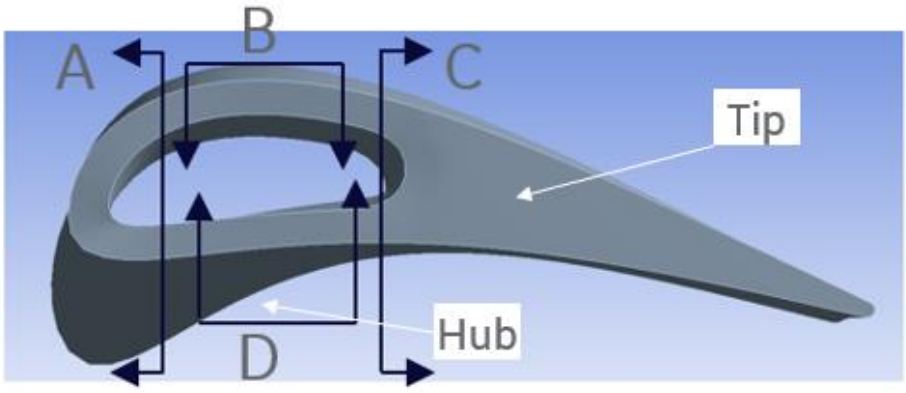

Figure 3.005: Single cavity airfoil section view orientations (top-down view)

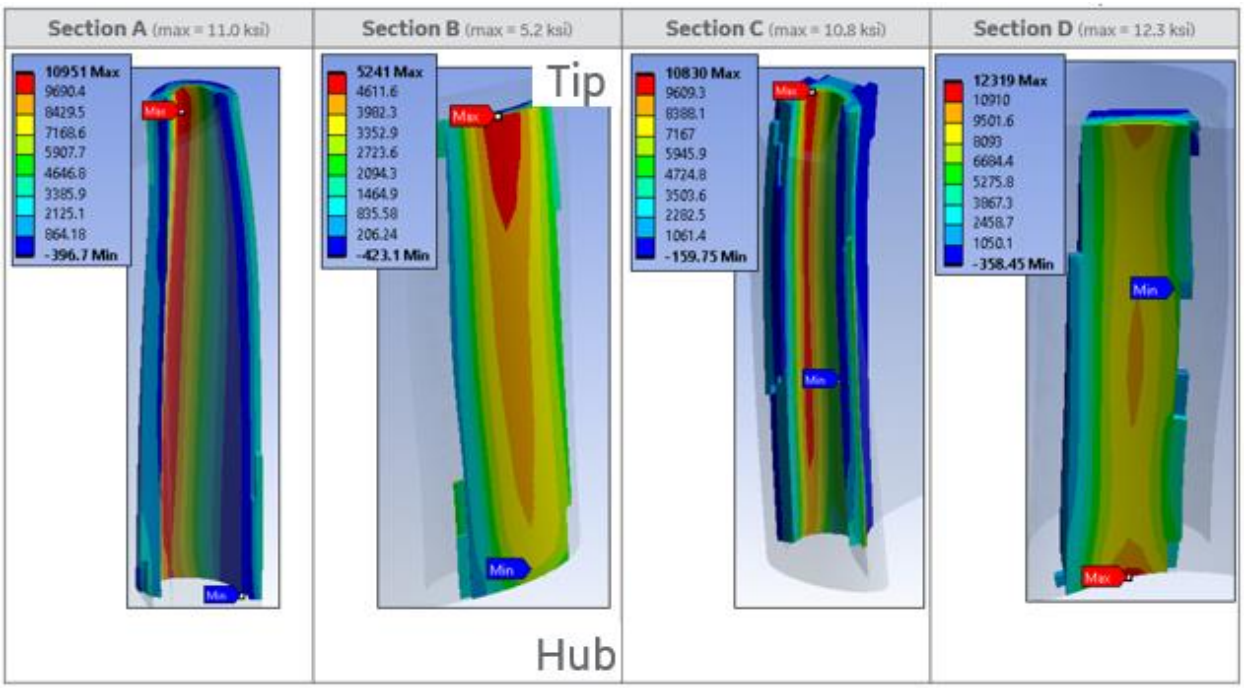

Figure 3.006: Contour plots of first principal stress for a single cavity airfoil

The single cavity airfoil exhibits high bending stresses near the lead edge and trail edge radii of the cavity, as well as the pressure loading causing high stresses at the mid-panel region of the cavities (Figure 3.006). Another metric to be evaluated is the interlaminar tension stresses of the configuration.

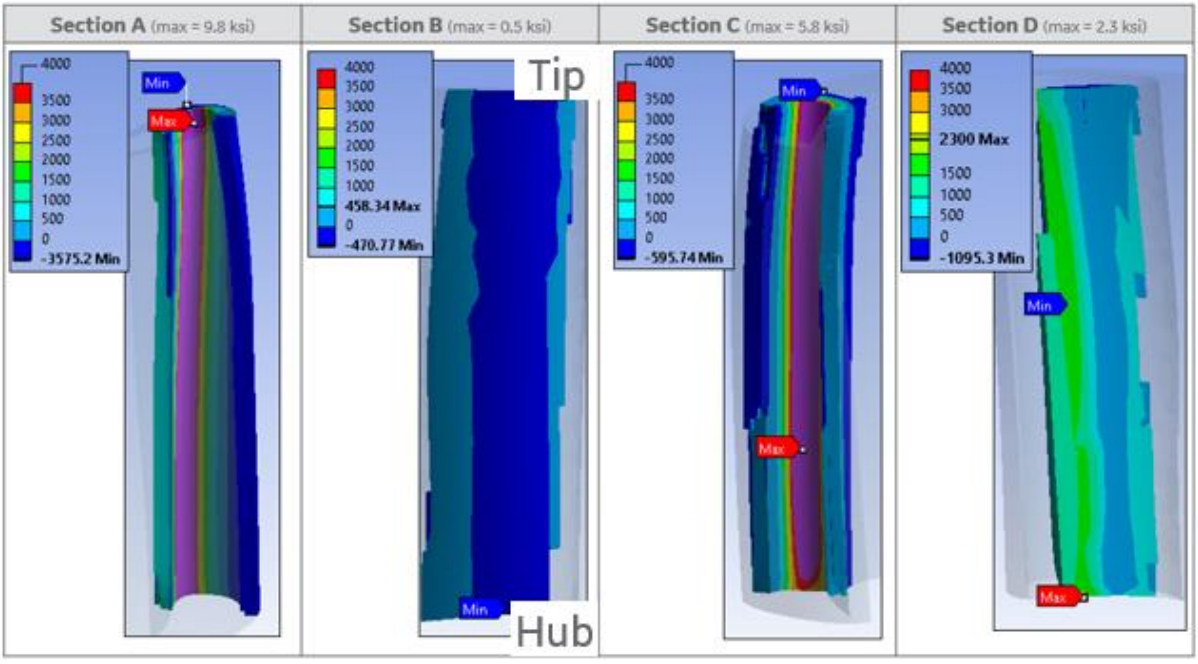

Figure 3.007: Contour plot of interlaminar stresses, oriented with the laminate through thickness direction.

In the interlaminar stress plots (Figure 3.007), a maximum interlaminar stress of 9.8 ksi occurs at the lead edge of the airfoil. A similar assessment was also performed for the double cavity airfoil, with the noted exception being the difference in pressure application as the aft cavity does not need to supply air to locations of the airfoil surface located in high static pressure regions of the airfoil. Stress contours are plotted with the section views shown below in Figure 3.008.

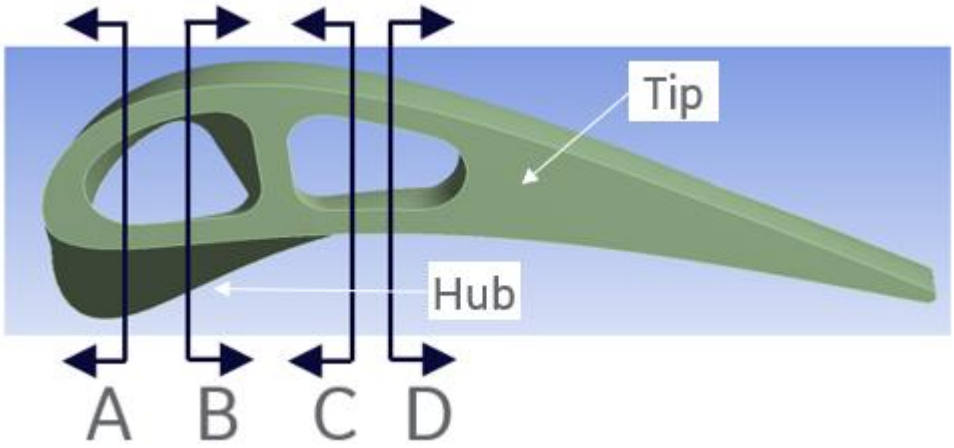

Figure 3.008: Section view notation for the double cavity airfoil (top-down view)

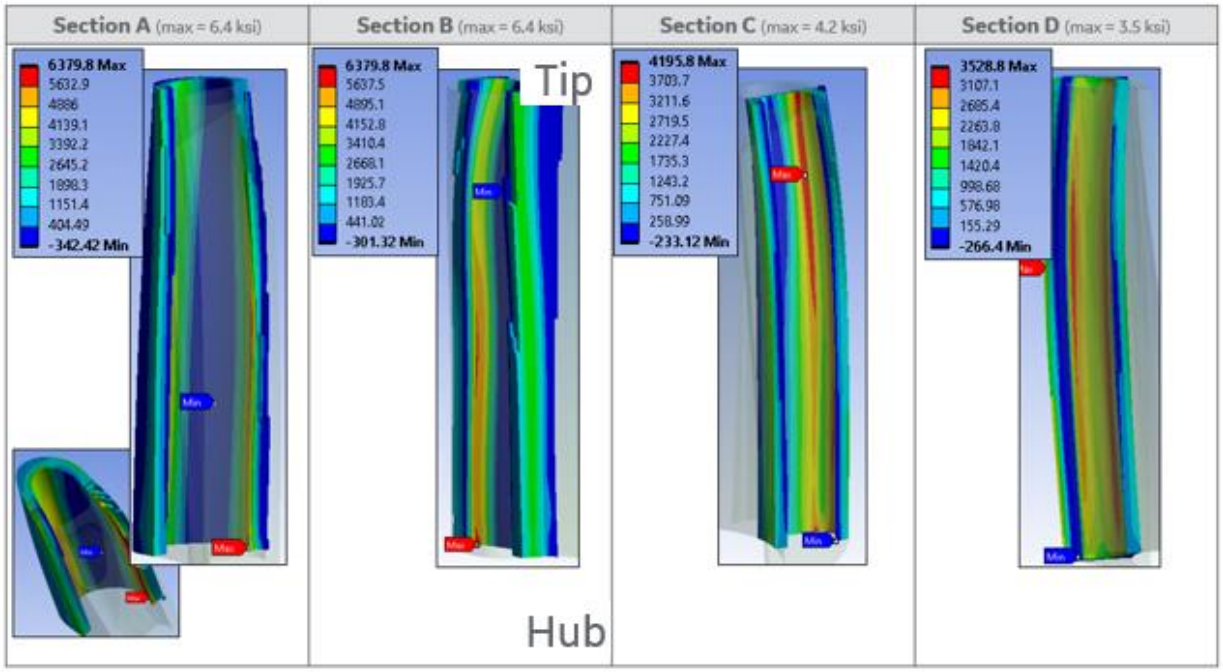

Figure 3.009: Contour plots of first principal stress for a double cavity airfoil

Compared to the single cavity airfoil a lower stress is observed throughout the cavity. The limiting location shifts from the mid-panel wall location (as observed on the single cavity airfoil) to the aft fillet regions of the forward cavity (Figure 3.009). In the interlaminar section plots a similar trend is viewed when comparing Figure 3.007 to Figure 3.010.

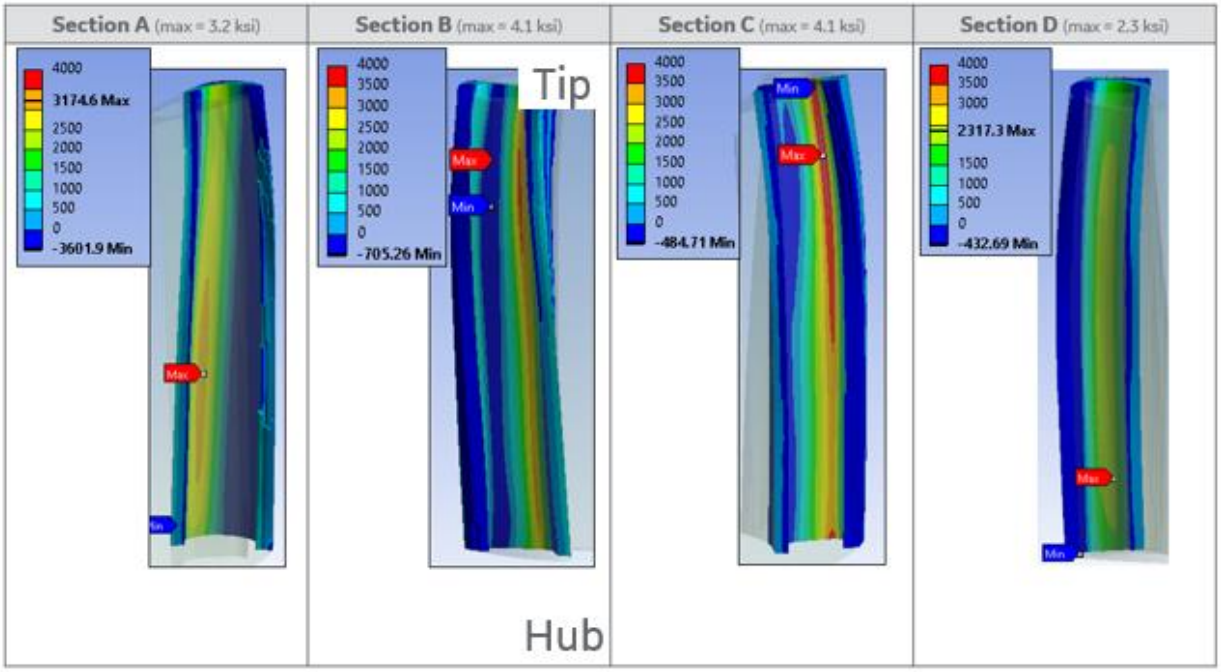

Figure 3.010: Contour plot of interlaminar stresses, oriented with the laminate through thickness direction.

The peak interlaminar stress region (when constructed as flat ply stack) lies within the rib between the cavities. While the double cavity configuration does represent a reduction in interlaminar stresses from the single cavity configuration, the interlaminar stresses still exceed an empirically derived screening criterion. This indicates that wrap plies will be required in the cavities to maintain structural integrity of the component. The presence of wrap plies lining the cavities for pressure capability will introduce a design and manufacturing constraint on the development of the airfoil because features that may induce damage to the fibers (small bend radii) must be avoided. The manufacturing constraints are also considered with respect to the thermal design of the blade test article, as the cavity wrapping will leave a significant portion of the aft section of the airfoil without internal cooling features. The CMC airfoil features an airfoil wedge angle sized to allow the cavities to be placed as far aft as possible, reducing the distance film cooling would be required to persist on the airfoil flowpath surface to reach the trail edge.

With consideration for the mechanical loading, a wall thickness taper was implemented from the airfoil hub to the tip as shown in Figure 3.011 below.

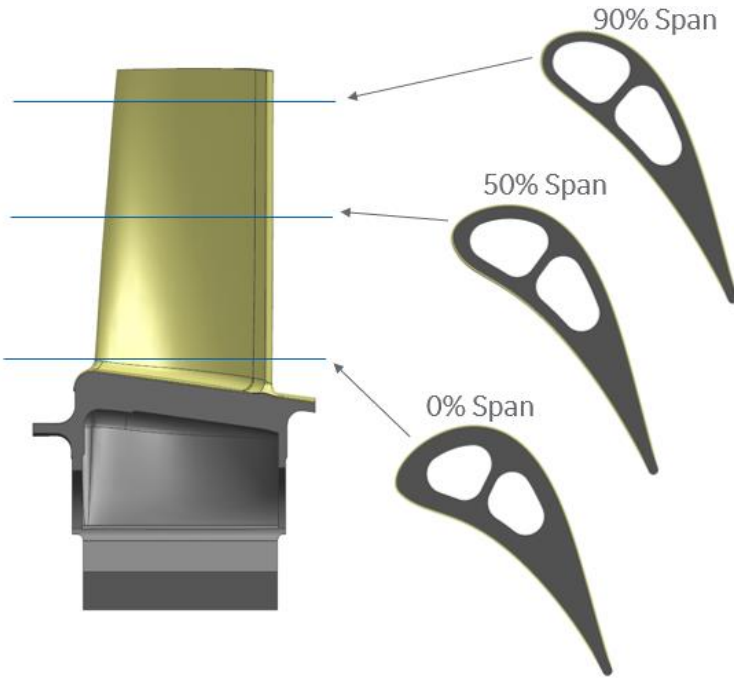

Figure 3.011: Airfoil cross-sections depicting wall thickness taper

As the wall thickness decreases from the root of the airfoil to the tip, the cavities also increase in cross-sectional area as they progress radially through the airfoil. This reduces the mass at outer spans of the airfoil, which has a strong influence on the rotational inertial load of the component.

The final component of the airfoil design is the sealing of the cavities at the tip of the airfoil. Historically, metallic turbine blades sealed the tip of the cooling passages using a welded "tip-cap" feature. Modern metallic turbine blades utilize casting cores that enable an integral tip to be cast in the same manufacturing step that the airfoil and the rest of the blade is produced. Since the CMC blade will require an internal mandrel during the autoclave consolidation an integral configuration would present manufacturing challenges, even when utilizing a consumable mandrel.

The approach pursued for the tip sealing involved the insertion of CMC tip-plugs, constructed from a flat laminate and machined to shape in the green-state, post consolidation of the tip plug laminate. The tip-plug laminates would be placed into the airfoil following the primary consolidation of the airfoil. After being placed into the blade preform the airfoil and tip-plugs would be line drilled and CMC pins consisting of rolled unidirectional pre-preg would be inserted through the tip. The configuration is shown below in Figure 3.012.

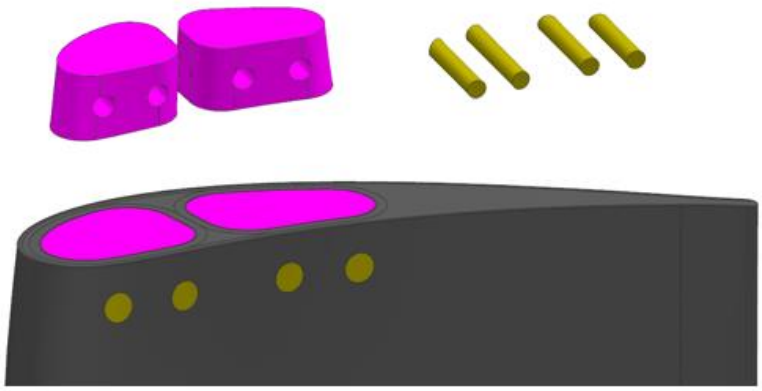

Figure 3.012: CMC tip plugs (magenta) inserted into the airfoil tip, and then mechanically retained with unidirectional pins (yellow).

After assembly the blade tip would then be consolidated and co-processed through all subsequent thermal processing steps in the manufacturing process. The CMC pins are utilized as additional mechanical retention of the tip plugs to add to the design robustness should the bond between the tip-plugs and airfoil laminate be compromised. To validate the CMC pin approach seven CMC pins were constructed and tested under monotonically increasing load at room temperature in a double shear metallic fixture with no bonding. The load - strain plots are shown below in Figure 3.013.

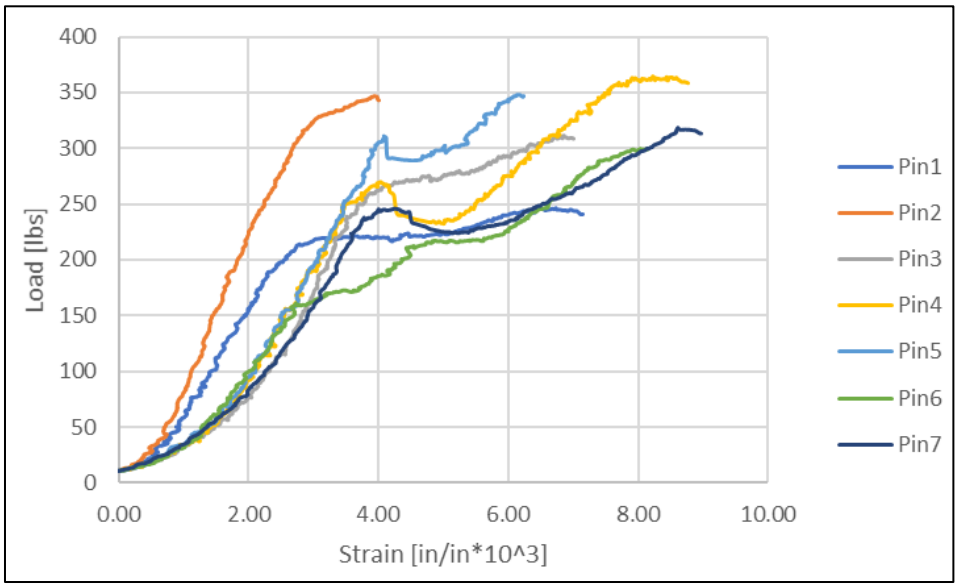

Figure 3.013: Load vs Strain trends of CMC pin double shear testing

All pins observe linear behavior to a minimum of 150 lbf of measured load, above which nonlinear effects are observed. When comparing to the required design space for the baseline test article, which has a maximum design load of 83.6 lbf at limit conditions a 44% load margin is observed. The pin shear data is shown in Figure 3.014 along with the design configuration of the baseline NASA test article.

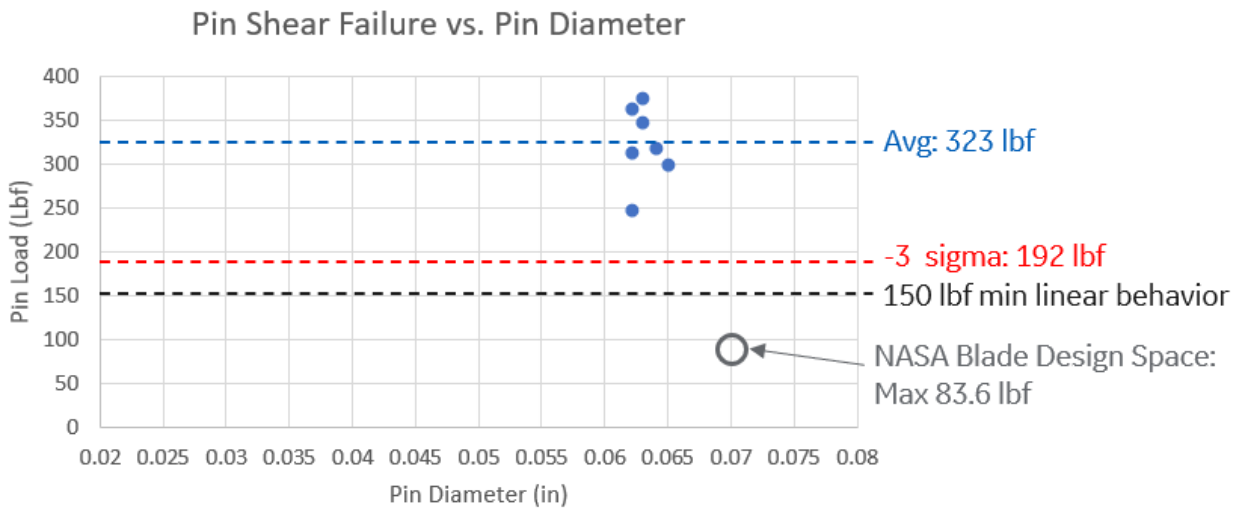

Figure 3.014: CMC Pin Shear Failure data

It is also noted that the pins were evaluated with computed tomography (CT) inspection prior to testing (Figure 3.015). It was observed that dimensionally all pins were not completely round, and that a subset of the pins tested contained voids as a product of the manufacturing process (which is included in the represented data set).

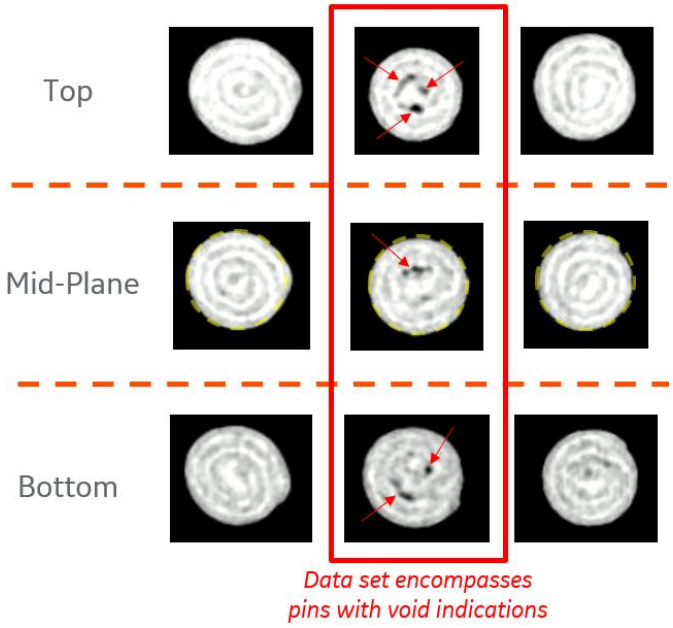

Figure 3.015: CT scan images of a 3 sample CMC pins

3.3.2 Attachment Design

The blade attachment for the CMC blade test article uses a single tang axial dovetail form which is typical of a CMC blade. This configuration is preferred to eliminate adverse loading conditions with the disk due to the mismatch in coefficients of thermal expansion. One challenge that arises

from a single tang dovetail definition is that more circumferential space is required on the rim of the disk for a given load and material capability. A view of the configuration is provided in Figure 3.016.

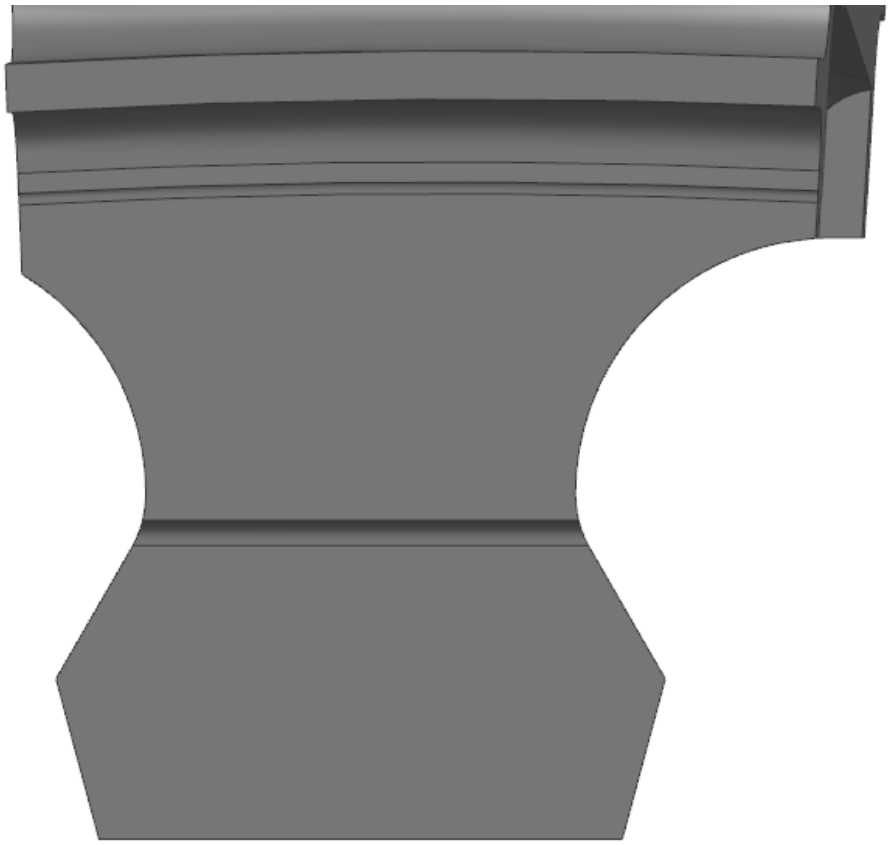

Figure 3.016: Dovetail configuration viewed normal to the dovetail skew angle

A key driver in the design of the dovetail attachment for the blade test article is to provide sufficient cross-sectional area to reduce net section and concentrated stresses to a level within the material capability. For a cooled CMC blade, the inclusion of cooling passages within the laminate structure presents an additional design challenge by introducing additional tooled surfaces and dimensional restrictions that limit the ability to effectively package a suitable shank-dovetail transition. In addition to the blade design parameters the disk interface also drives the design space available to the configuration of the blade; as the blade attachment feature cannot occupy a design space that compromises the integrity of the disk posts. For the development of the CMC blade test article the configuration of the stage 1 high pressure turbine rotor configuration was maintained from the metallic benchmark (blade count and rim axial length). The design approach for the CMC blade test article prioritized maintaining a reasonable net section stress distribution through the blade shank while also appropriately sizing the pressure faces for the high contact stresses at the disk interface. One feature common to GE's CMC blade dovetails that enable this is an axial skew

of the dovetail (Figure 3.017), which serves two purposes for the layout of the attachment; it reduces the transition of the plies from the dovetail to airfoil by bringing the aft portion of the dovetail closer to the trail edge of the airfoil, while also increasing the cross-sectional area of the shank for a given thickness.

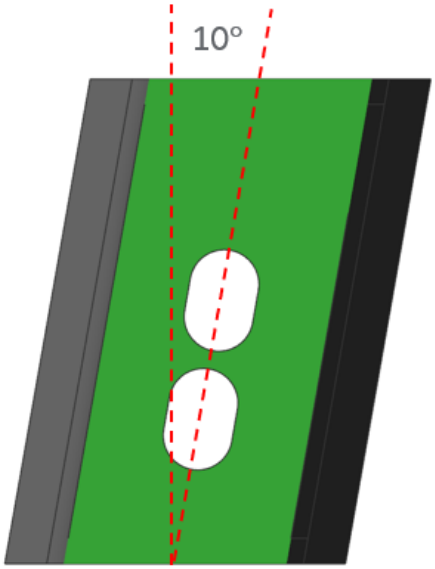

Figure 3.017: Example of a 10° dovetail skew

For the configuration of the blade test article a 10° skew relative to engine axial was implemented. Typically, a dovetail skew is avoided on turbine blades as it introduces edge loading onto both the blade and the disk post; however, a CMC blade mitigates some of that impact with a lower inertial loading resulting from a relatively lower density compared to the nickel-based alloys typically utilized in the high-pressure turbine. With the dovetail form and skew angle selected, an iterative process is carried out to produce an acceptable interface consideration. As the primary objective of the program is focused on the CMC blade and its design parameters, only fundamental rotor attachment criterion were evaluated such as: disk post net section stress, disk post tang shear and disk post overturning moments. Figure 3.018 below depicts the resulting configuration from the attachment optimization.

Figure 3.018: Representative Blade-Disk interface design

The key parameters that were determined while optimizing the dovetail configuration were the: pressure face spacing, pressure face length and shank fillet radius. The pressure face spacing combined with the dovetail flank angle and pressure face length establish the min-neck region of the shank, or the minimum cross-sectional area located above the pressure faces. This location is where the peak net section stresses in the blade are observed. Figure 3.019 depicts the net section stress distribution though the span of the blade test article.

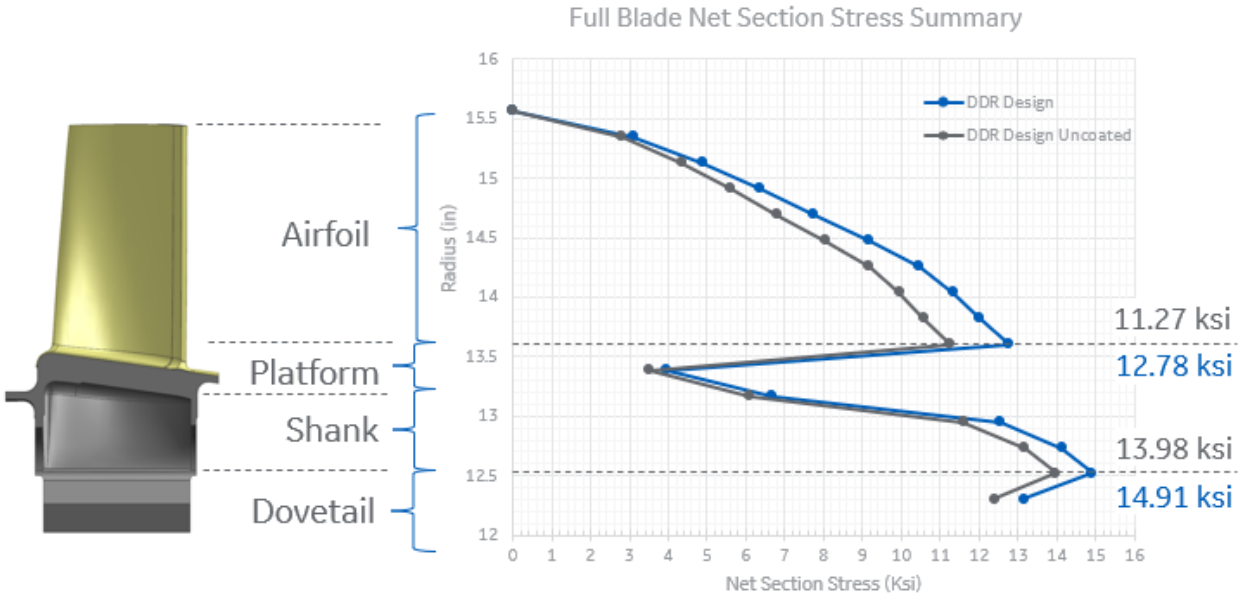

Figure 3.019: Blade test article net section stress plot.

For the design of the CMC blade test article a maximum net section stress of 14.91 ksi (for the coated blade configuration) is observed at the min-neck of the dovetail. This net section stress does account for the added mass of the EBC coating on the component, but does not take credit for any mass reduction resulting from the manufacturing of the cooling holes.

Another consideration evaluated for the attachment design is the average contract stress (crush stress Table 3.002) of the pressure face interface with the disk post. The crush stress metric, relative to CMC blades, informs the design risk relative to accumulating damage and wear local to the pressure faces and evaluates the blade radial load acting on the projected area of the blade pressure faces

Table: 3.002: Average crush stress calculation parameters

AVG Crush Stress Parameters		
Limit Speed	13,000	RPM
Limit Speed	1,361.36	rad/s
Total Load	15,939	lbf
Common Contact Length	0.112	in
Break Edge	0.0075	in
Average Crush Stress	54.02	ksi

The average crush stress on the pressure faces of the blade can be directly calculated using the following formula:

$$\text{Average Crush Stress} = \frac{Blade\ Radial\ Load}{(2*common\ contact)*\frac{(axial\ length-2*break\ edge)}{\cos(skew\ angle)*\cos(inc.\ angle)}} \qquad (1)$$

For the cooled blades test article, the dovetail axial length and attachment profile are shown below in Figure 3.020.

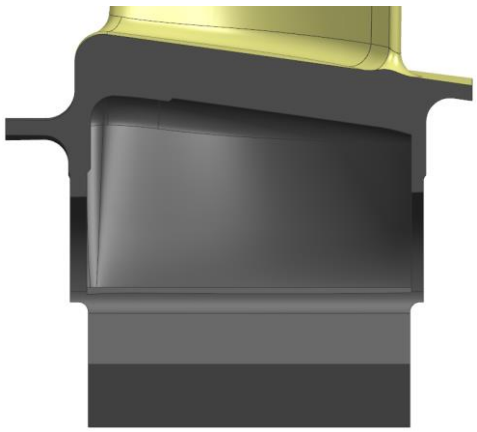

Figure 3.020: Attachment Profile view indicating dovetail axial length

The resulting average crush stress for the CMC blade test article configuration is 54.02 ksi which lies outside of GE's experience for solid CMC blades. To bring the average crush stress levels within prior experience an extended pressure face length would be required, but additional space would be limited without compromising the integrity of the disk post. To gain the needed surface area with the maximum pressure face length permitted an extension to axial length would also be required, potentially resulting in a hardware packaging issue with the current layout of the turbine.

3.3.3 Dovetail Pull Test Article Design

To validate the sizing of the CMC blade dovetail attachment a dovetail "pull-test" coupon was designed to exercise a representative cooled blade attachment architecture monotonically to inform the failure mechanisms and capability of a cooled CMC dovetail attachment architecture. The design of the dovetail pull-test specimen occurred in parallel to the blade test article and shares the architectural and configuration commonality with the blade. Figure 3.021 shows an overview of the dovetail pull test specimen.

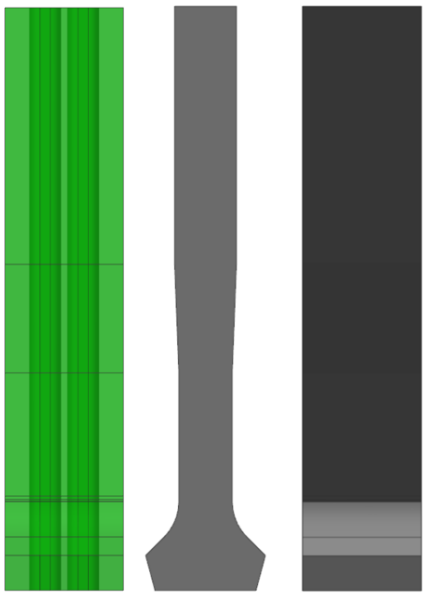

Figure 3.021: Dovetail pull test specimen overview with transparent view to highlight cooling passages

A key requirement for the design of the dovetail pull test specimen was that failure needed to be achieved within the 15,000 lbf calibrated load capability of the test frame. To achieve this the dimensions of the test specimen were scaled relative to the blade test article, but consideration was given to ensure that feature parity/similarity with the blade test article was maintained, Figure 3.022 depicts the cross-section of the blade shank min-neck compared to the dovetail pull test specimen min-neck.

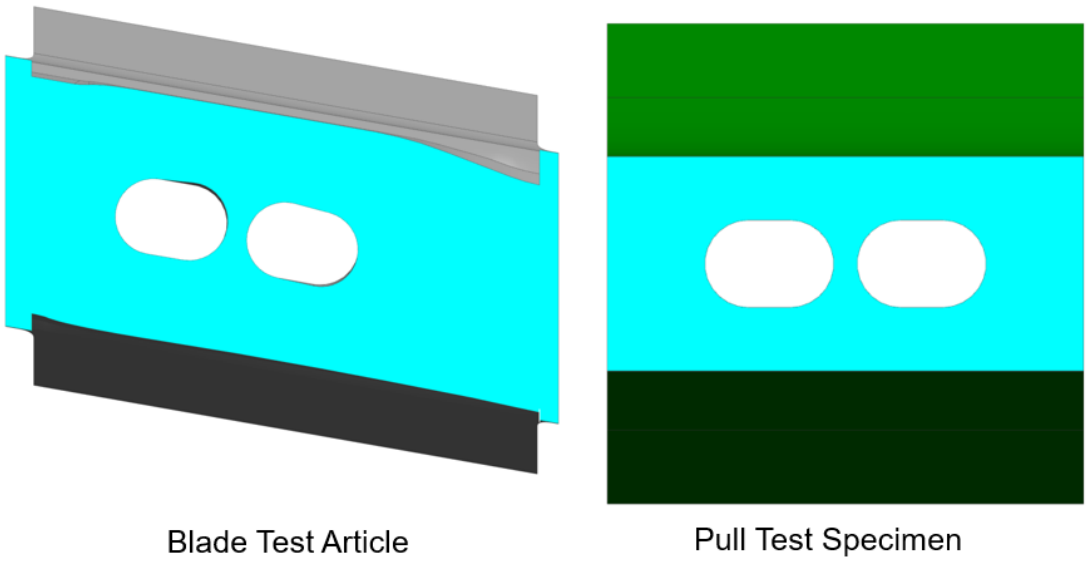

Figure 3.022: Min-Neck region cross-section comparison between the blade and dovetail pull-test specimen

3.4 Baseline Blade Test Article Thermal Design

The thermal design of the blade test article was conducted by leveraging external boundary conditions representative of a steady state high power condition of the GEnx engine benchmark. External pressures were generated from the aerodynamic design solution of the CMC airfoil. The thermal model includes convection, conduction and radiation modes of heat transfer, and uses full blade finite element model to develop temperature predictions.

The thermal design configuration of the CMC blade test article encompasses the integration of an environmental barrier coating (EBC), internal cooling circuit and film hole configuration to achieve an acceptable thermal design operating in engine relevant conditions.

3.4.1 EBC Coating Definition

SiC/SiC ceramic matrix composites are susceptible to interactions with water vapor present in combustion gases at high temperatures. To mitigate the susceptibility to CMC recession, a slurry based EBC coating was applied to the blade. The coating consists of a bond coat and a rare earth di-silicate topcoat. Figure 3.023 shows the coverage of the proposed EBC coating.

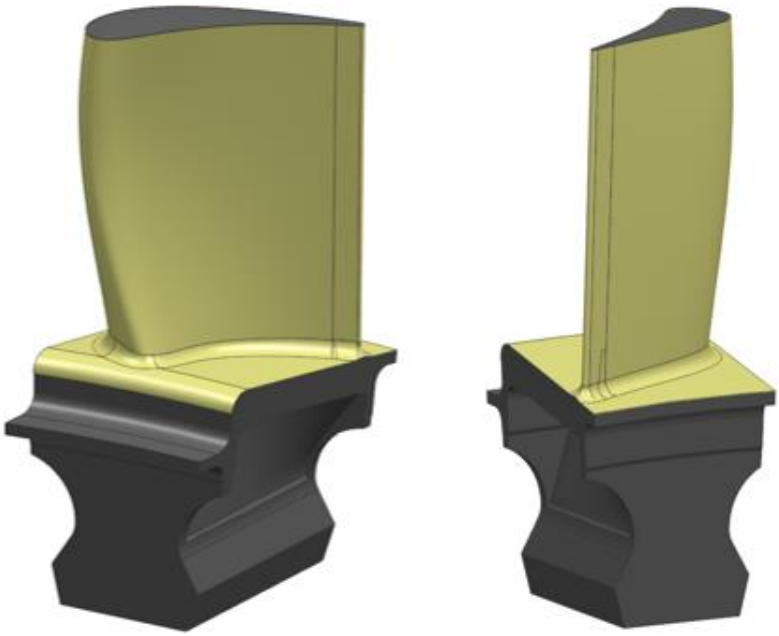

Figure 3.023: EBC Coating definition / Coverage

The EBC coating provides coverage to all flowpath surfaces with the exception of the blade tip. Coating application is masked on the platform slashfaces and the forward tangency transitioning to the angelwing seal.

3.4.2 Thermal Features Configuration

As discussed in prior sections the CMC blade test article utilizes a simplified radial passage cooling circuit augmented by film cooling.

Supplementing the internal supply passages, the blade contains lead edge showerhead cooling holes, pressure side and suction side cooling with shaped diffusers, trail edge ejection cooling, and local tip cooling (Figure 3.024). The surfaces of the radial cooling passes themselves are smooth wall (CMC matrix) and do not contain any heat transfer coefficient enhancing features.

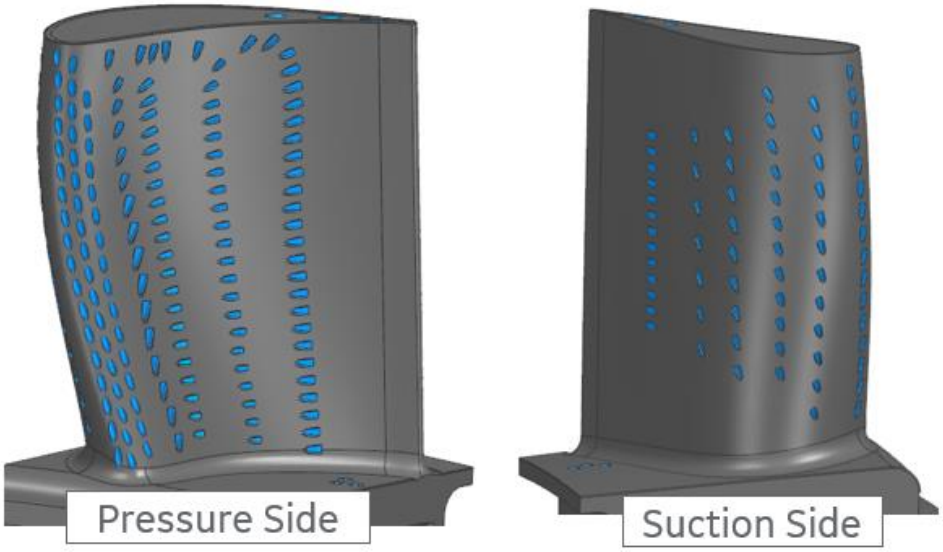

Figure 3.024: Pressure Side and Suction Side images of the airfoil cooling pattern.

The cooling holes at the lead edge of the test article consist of three rows of conical showerheads. The pressure side of the airfoil contains four rows of shaped diffusers with an additional seven shaped cooling holes locally placed near the tip of the airfoil. The suction side of the airfoil contains six rows of shaped diffuser cooling holes.

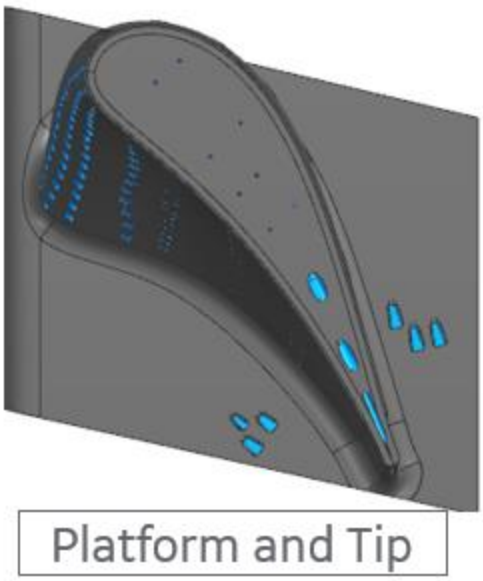

Figure 3.025: Top-down view of the platform and tip cooling

Both the pressure side and suction side of the blade platform include three shaped diffuser holes. The tip of the blade contains eight cylindrical holes for bore cooling above the cavities and two conical holes plus an asymmetric fan hole near the trail edge (Figure 3.025).

3.4.3 Thermal Results

Figure 3.026 shows the temperature distributions predicted by the thermal analysis for the blade test article on the exterior surface of the EBC.

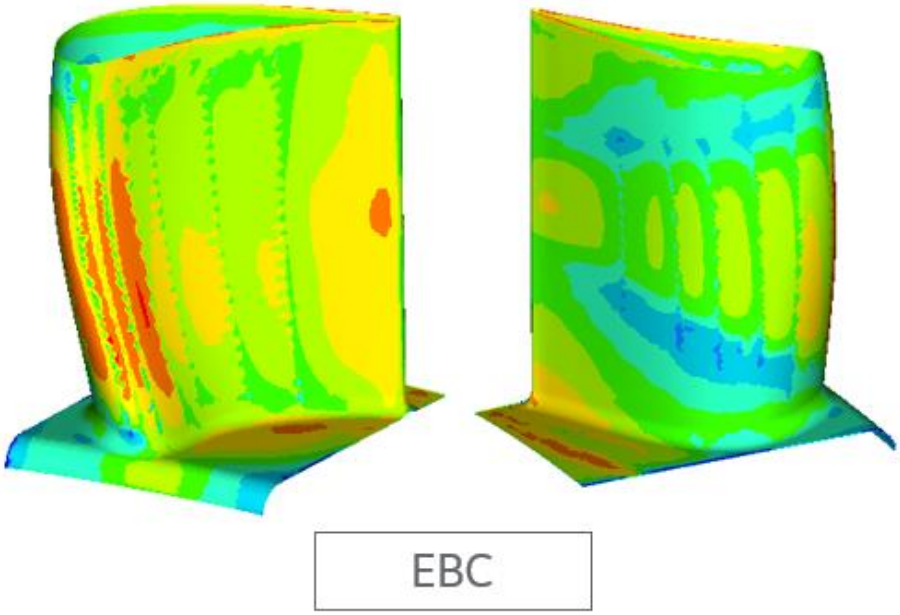

Figure 3.026: Thermal contour plots of EBC temperatures

The peak EBC temperature occurs on the pressure side of the airfoil, near mid-span, just aft of the last row of conical holes. Another region of locally high temperature is located near the trail edge of the airfoil near mid-span. All locations on the EBC are within the GE's recommended EBC temperature limits. The CMC temperatures are shown below in Figure 3.027.

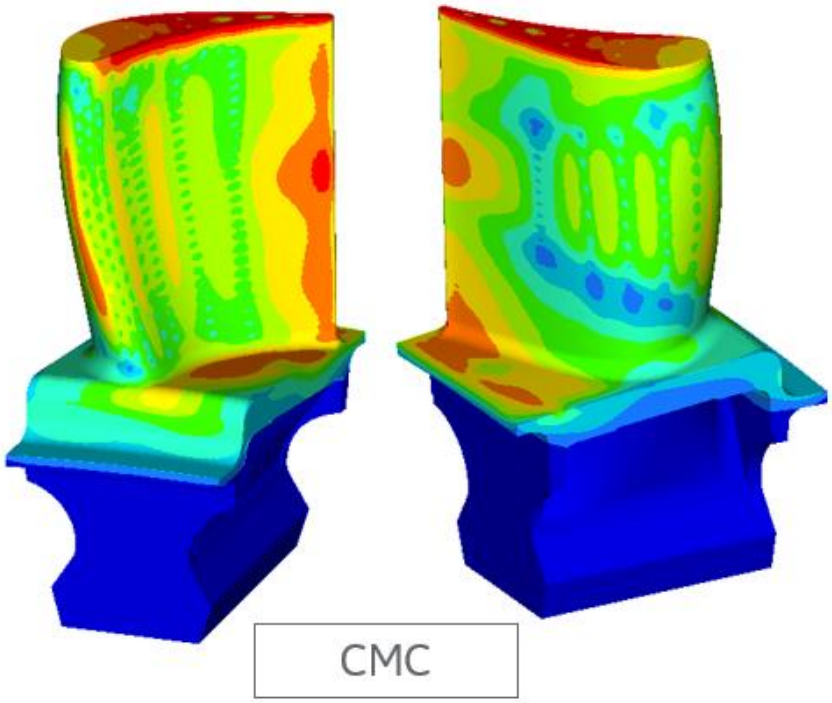

Figure 3.027: Thermal contour plots of CMC temperature

With the exception of a local region on the tip of the blade all locations on the blade meet the recommended use temperature for the CMC. Outside of the tip region, the highest observed temperature is at the pressure side trail edge of the airfoil. The region of the tip that exceeds the recommended use temperature is driven by the lack of internal cooling on the airfoil and the inability to place a cooling hole local to the pressure side region.

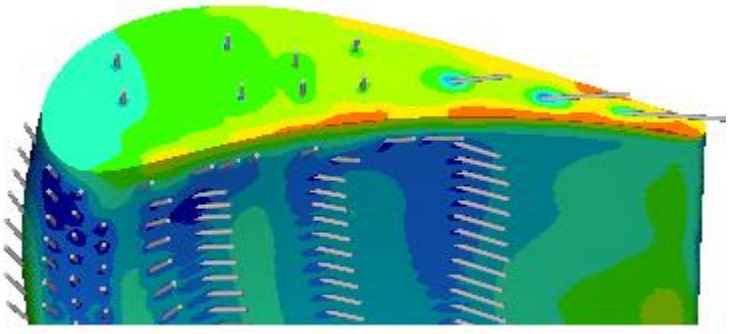

Figure 3.028: Refined thermal contour of the blade test article tip region.

In Figure 3.028 above, the local maximum can be observed where the edge of the airfoil pressure side surface meets the tip of the airfoil near the trail edge. This location on the pressure side rail of the tip is not receiving a benefit from the tip cooling. Due to the limitations on the cooling hole placement, there is also no pressure side cooling located near the trail edge to carry film over the tip of the airfoil.

3.4.4 Thermal Design Conclusion

Most of the blade test article meets EBC and CMC use temperatures. The notable exception is a local region located on the pressure side rail of the tip of the blade near the trail edge. An abatement was identified but is not compatible with the current cooling architecture of the component. Continued efforts for cooled CMC blade development should focus on cooling architecture development that can adequately cool the aft portion of the airfoil.

4.0 Task 2 – Test Article Fabrication

4.1 Objective

The objective of Task 2 was to fabricate CMC test articles to be tested by NASA. The test article consists of a dovetail architecture and cooling passages representative of that of a cooled CMC turbine blade. Two manufacturing techniques were utilized to create the cooling passages, namely a hand wet layup, and green state machining. A quantity of four were delivered for each configuration, for a total of 8 test articles. The manufacturing process, from preform definition through machining and inspection, is summarized in Section 4.2 below.

4.2 Manufacturing Approach

To prepare for manufacturing, the nominal test article was scaled at least 0.25” in the in-plane direction to create a stock on condition for final machining (Figure 4.001).

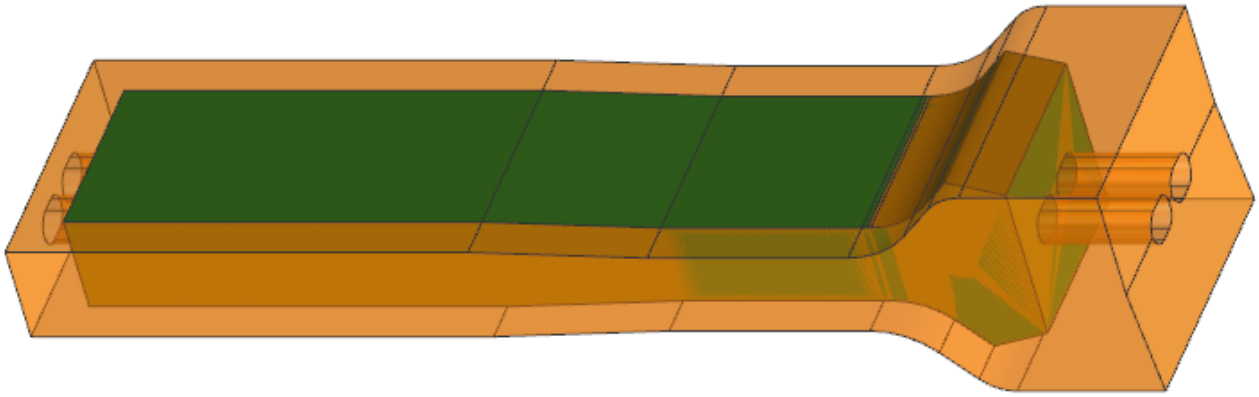

Figure 4.001 – Test Article Preform and Machined Bodies

From the solid body, sheet bodies were created for each ply to fill the volume of the preform, shown in Figure 4.002. Sheet bodies are grouped into laminates and color coded for differentiation.

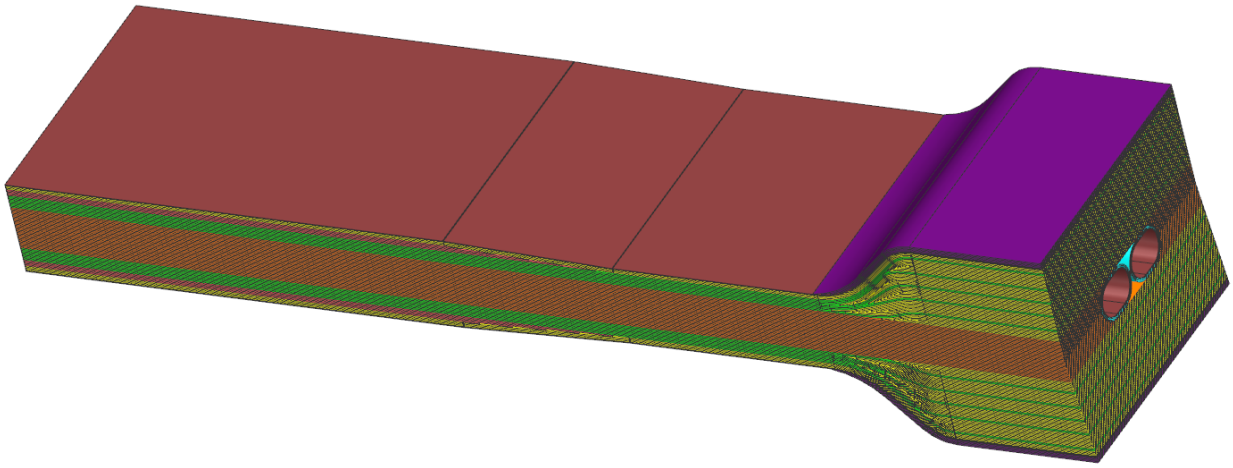

Figure 4.002 – Test Article 3D Sheet Bodies

From the 3D model, sheets were then flattened into 2D shapes using FiberSim to produce ply shapes for cutting fiber prepreg tapes. These ply shapes are arranged within the area of a prepreg tape and oriented to control fiber direction. Each ply is labeled with its respective laminate and number in the layup sequence. A majority of plies are rectangular, with long strips for wrapping the cavity mandrels. Examples of ply shapes for a flat laminate ply and mandrel wrap plies are shown in Figure 4.003.

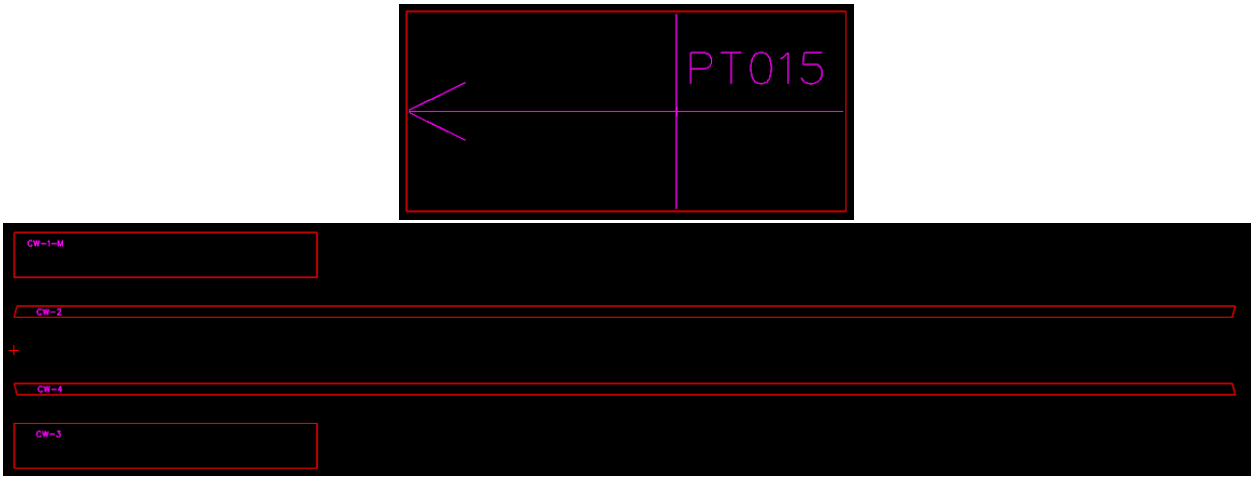

Figure 4.003 – Example Flat Pattern Ply Shapes

The Melt Infiltrated (MI) SiC/SiC test articles were manufactured with the same general process as used for turbine components, detailed below in Figure 4.004. The 2D flat patterns are digitally laid out to control ply fiber direction within the area of a prepreg tape, and then automatically cut. These plies are then laid up on hard tooling to define the outer mold line (OML). The part and tooling are then processed through an autoclave to laminate and consolidate the preform. The part

is then processed through pyrolysis to convert organics, and finally melt infiltration to infiltrate with Si and react to create a SiC/SiC preform. Once infiltrated, the preform passes through dimensional and NDE inspections, final machining, and a final dimensional and microstructure inspection.

Figure 4.004 – MI SiC/SiC Composite Manufacturing Process

Specific to the dovetail test article was the creation of preform cooling passages. The test articles consisted of two manufacturing techniques to create the cooling passage, namely a hand/wet layup, and green state machining. Each technique required a unique set of flat pattern ply shapes. To produce the wet layup test articles, dovetail insert packs, detailed as yellow in the 3D sheet bodies, were laid up and pre-consolidated. After consolidation of insert packs, full body plies were laid up, alternating with insert packs, to produce a flat stack across the width of the test article, up to the interface with the cooling passages. At this point, the plies split to create the profile of the cooling passage assembly. The process was repeated to create two halves, each with a channel for the cooling passage, detailed in Figure 4.005.

Figure 4.005 – Wet Layup Cavity

Similar to the wet layup, green state machined articles were laid up as two flat stack halves. Rather than splitting plies to create the channel, plies were continuous across the width of the article, up to the midplane. These flat stacks were then partially cured to remove solvents and stiffen the green state preform. Using a CNC machine, the cavities were machined out of each half to match the profile of the cooling passage assembly, as shown in Figure 4.006.

Figure 4.006 – Green State Machined Cavity

After cavity formation, mandrels were wrapped to create the final inner dimension of the cooling passages. A setup for a mandrel wrapping trial (*angle and ply shapes were later modified*) and a completed mandrel are shown in Figure 4.007 below. Fiber angle was controlled by chamfers on the end of the ply shapes and an alignment feature on the wrapping setup.

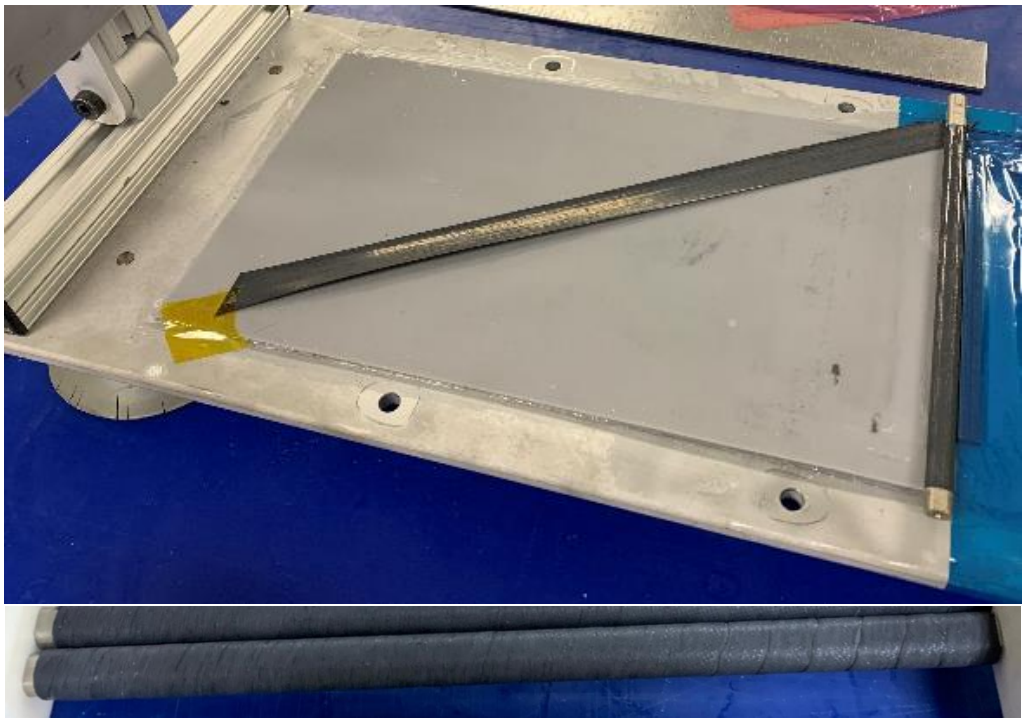

Figure 4.007 – Mandrel Wrapping

To fill the volume between the cooling passages and flat stacks on each side, two fiber noodles were rolled from prepreg plies, parallel to the fiber direction. The rolled noodles were then placed in a 3D printed tool with a release film and subjected to vacuum pressure to form the noodle shape, shown in Figure 4.008.

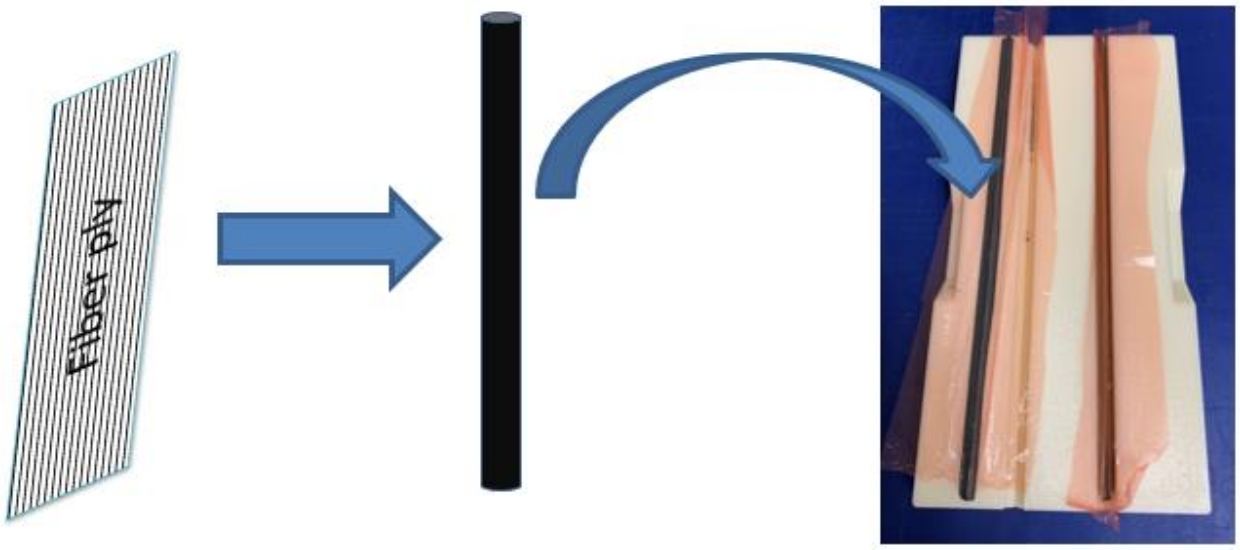

Figure 4.008 – Noodle Forming

After noodle forming and mandrel wrapping, they were assembled with a ceramic matrix slurry precursor. The slurry serves to tack the noodles in place, and fill any small volumes not occupied by a fiber ply. The assembled mandrel is detailed in Figure 4.009 below.

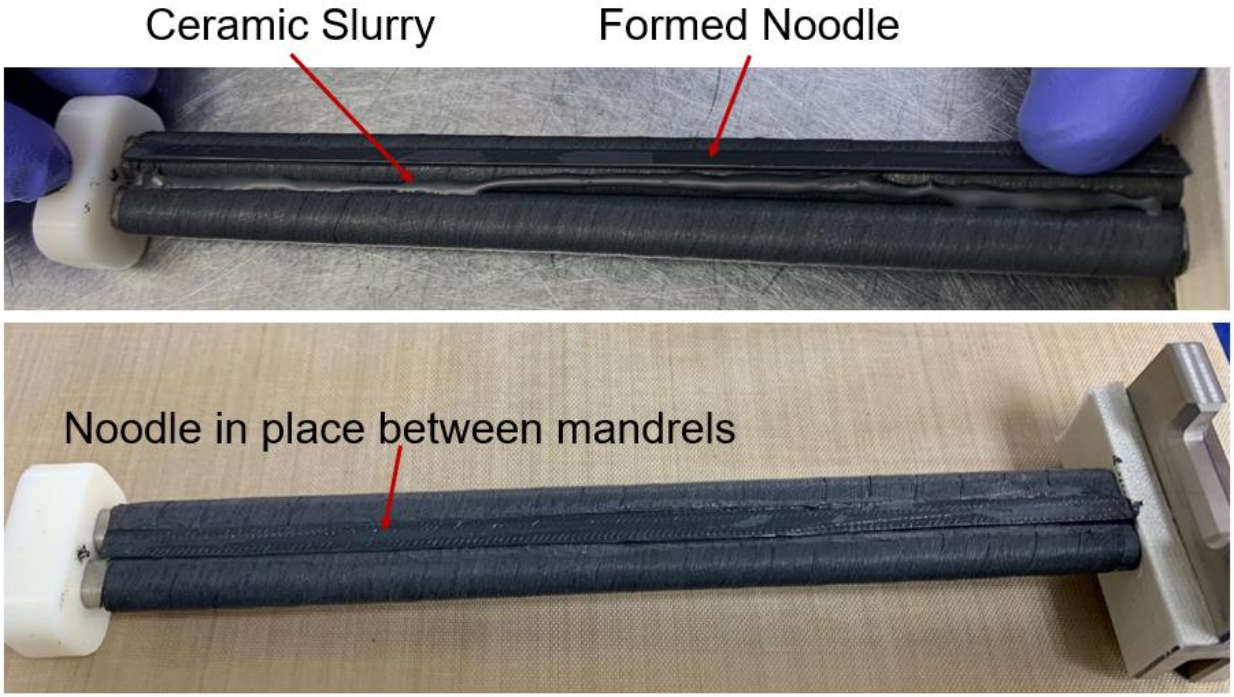

Figure 4.009 – Noodle Placement

The completed mandrel assembly was then placed in the cavity of one stack. Mating faces on hard tooling control assembly placement. To complete assembly, the second half is placed on top, detailed in Figure 4.010.

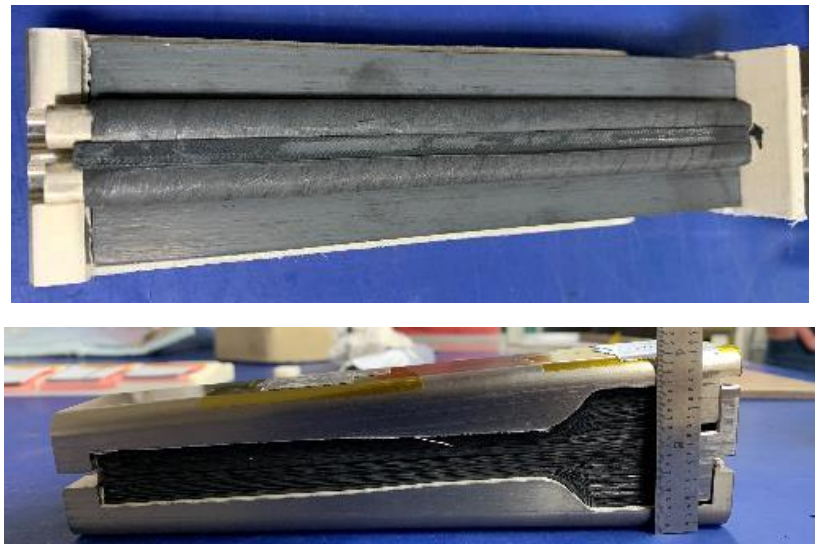

Figure 4.010 – Mandrel & Final Assembly

Upon assembly of the full preform, the part and tool were bagged for autoclave thermal processing, to consolidate and laminate the preform. A previously developed process model was utilized on the relevant geometry to define the thermal profile to arrive at target composition. Autoclave temperatures, dwell times, pressure magnitude and pressure application times were varied. Analytical outputs from the model predict solvent, binder, and plasticizer concentrations during and at the end of the thermal cycle. A cycle was selected to arrive at concentrations consistent with those in commercial engine hardware, which are favorable for lamination quality throughout thermal processing.

After autoclave, a subset of the initial preforms were inspected with computed tomography (CT) X-ray inspection to verify compaction and location of fiber plies. All preforms were then processed through pyrolysis to convert remaining organic material to carbon and create a porous network. Preforms were melt infiltrated, where molten silicon infiltrates the porous network and reacts with residual carbon to create a SiC matrix, and the final SiC/SiC composite. After infiltration, preforms were inspected with CT to verify infiltration and characterize any indications, shown in Figure 4.011.

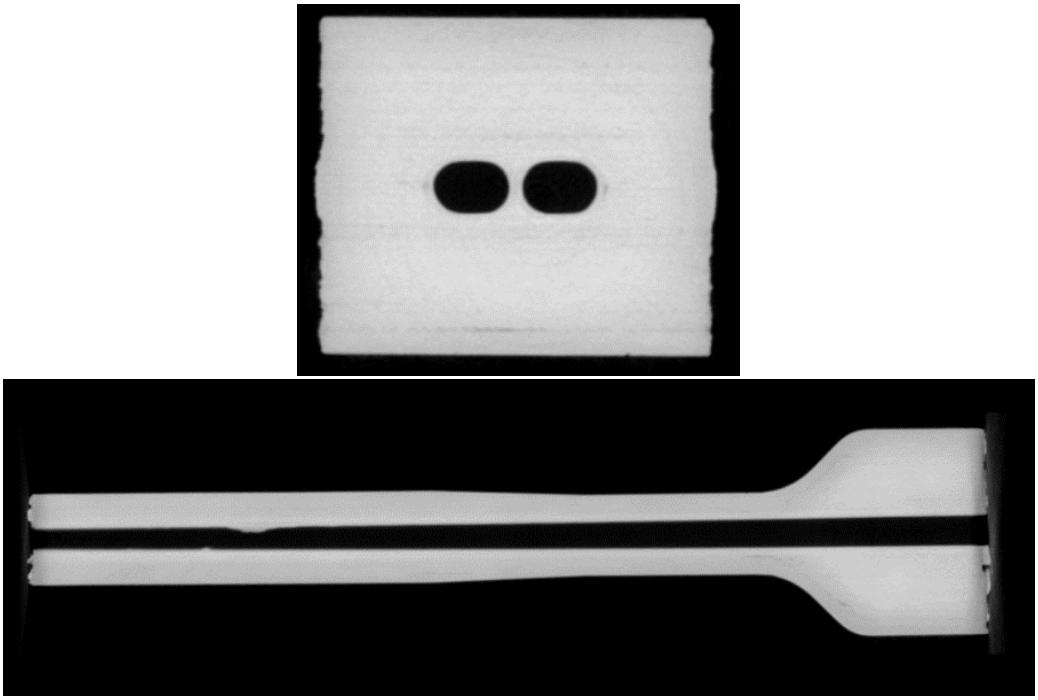

Figure 4.011 – Computed Tomography (CT) Inspection

A blue-light non-contact dimensional inspection was used to measure the geometry of the preform, shown in Figure 4.012. The plot shows the deviation, in 3D space, between the inspected article and the nominal definition.

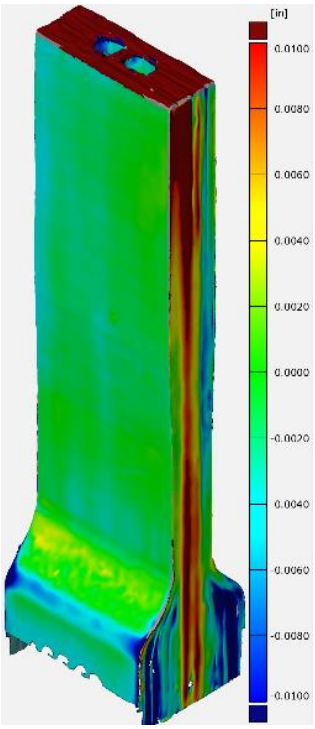

Figure 4.012 – Non-contact Dimensional Inspection

To prepare for final machining, preforms were mounted on a fixture and again inspected with blue-light. The data generated by the blue-light was then compared to the nominal fixturing definition. Offsets were created to account for any small deviations in placement and were inputs to adjust toolpaths to ensure proper cleanup, while avoiding machining of structural fiber, shown in Figure 4.013. Using these inputs, the parts were machined using diamond coated grind wheels, and a final dimensional inspection was performed to check overall dimensions and verify the alignment and profile of dovetail pressure faces.

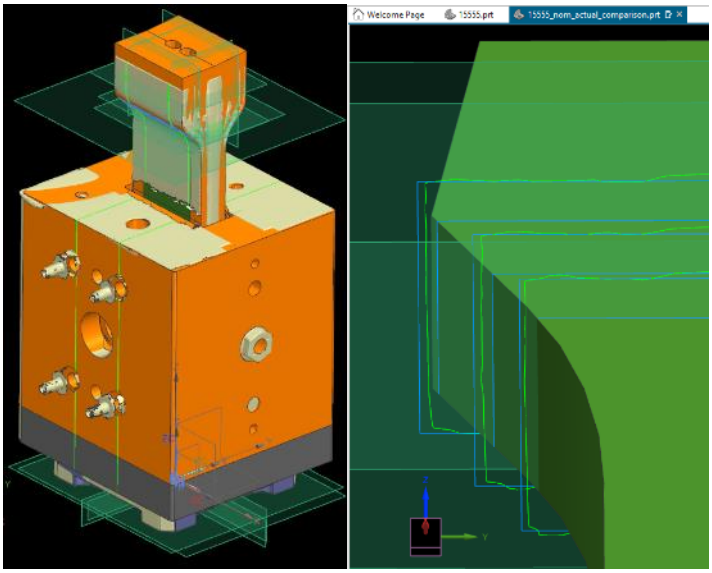

Figure 4.013 – Adaptive Machining

After all processing was complete, a microstructure assessment was performed on machined surfaces to evaluate lamination, infiltration, and material around the cooling passages, shown in figure 4.014.

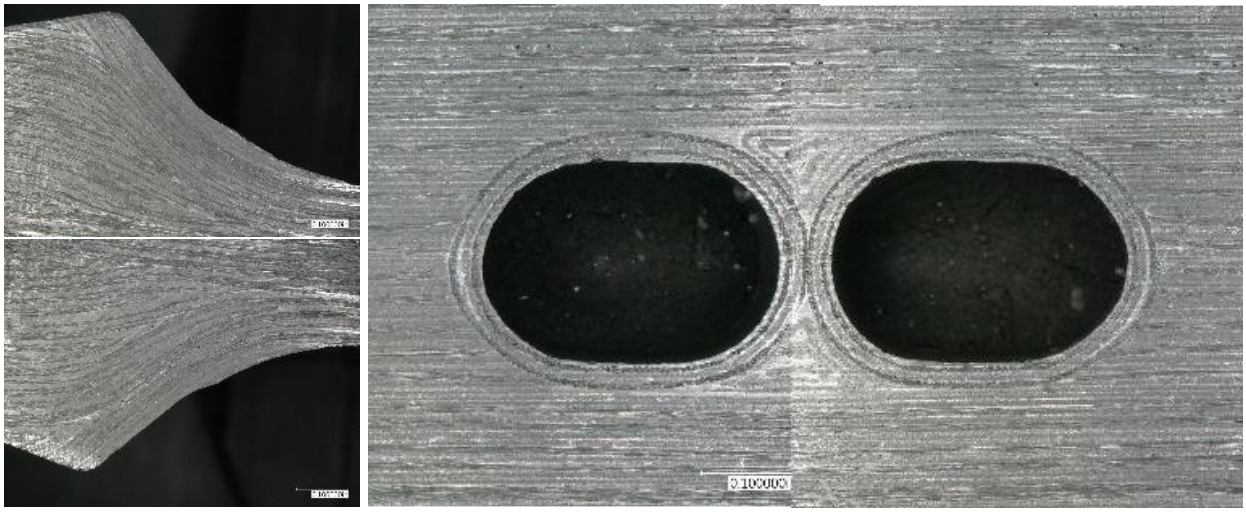

Figure 4.014 – Test Article Microstructure

Test articles were laser marked with their serial number for traceability prior to shipment. A completed article is shown in Figure 4.015 below.

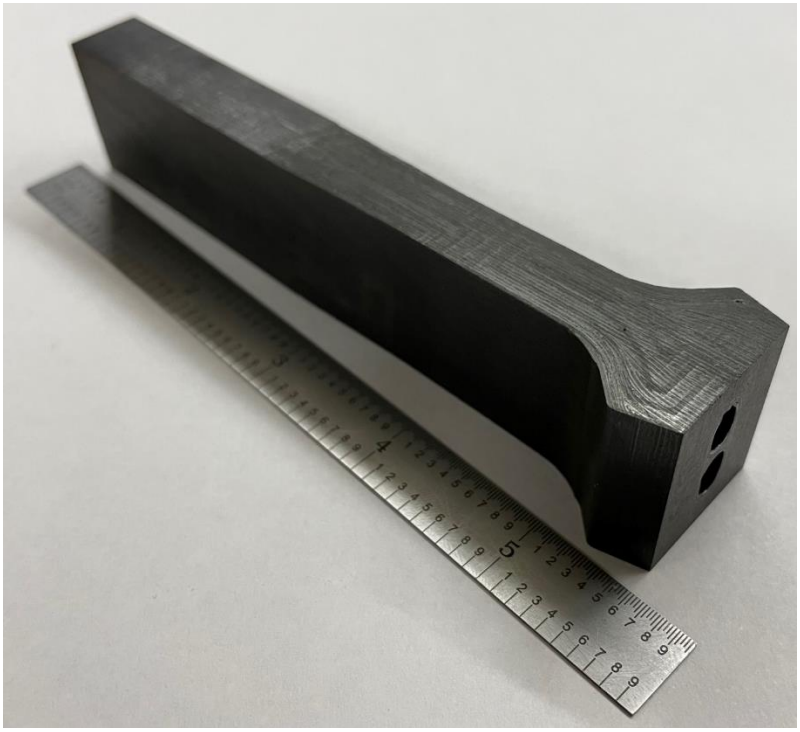

Figure 4.015 – Completed Test Article

5.0 Task 3 – Experimental Program

5.1 Introduction

As part of a series of low Technology Readiness Level (TRL) testing supporting cooled CMC Blade Technology several testing campaigns were completed in partnership with the NASA Glenn Research Center team. These tests included the following test programs:

- Cooled Blade Architecture Dovetail Pull-Testing
- HCF K_f testing of 2:1 biased laminate test specimen $m[0/90/0]_3m$ with and without cooling holes
- eSPLCF K_f testing of 2:1 biased laminate test specimen $m[0/90/0]_3m$ with and without cooling holes
- EBC Erosion and Impact Testing

Germane to the development of the blade test article, the dovetail pull test campaign is directly related to key failure mechanisms of the blade test article (Delamination, Shank fillet damage initiation, rib crush).

5.2 Dovetail Pull Test Program

5.2.1 Objective

The Dovetail Pull test is a TRL development test proposed to characterize the dovetail interlaminar tension (ILT) and load carrying capability for a novel cooled blade dovetail architecture. Learnings from the test will inform the methods and capability of the full-scale blade test article. Also included in the study is variation on manufacturing process to inform capability dependency relative to the implementation of the consolidation of the component around the cavity geometry.

5.2.2 Test Matrix

For the dovetail pull test, a total of eight specimen were planned – representing four replicates of two configurations.

Table 5.001: Dovetail Configuration Matrix

Temp.	Cavity Config.	Manufacturing Method	Test	# of Specimens
RT	Dual Cavity	Green Machine	Monotonic	4
	Dual Cavity	Wet Layup	Monotonic	4

As shown in Table 5.001 the major independent variable for the dovetail pull test is the variation of the manufacturing process. Half of the specimens will be manufactured using the wet lay-up process depicted in Figure 4.005 or the green machine process depicted in Figure 4.006. This will inform whether there is an impact of the as manufactured process to the capability of the dovetail configuration as a “product of the process”.

5.2.3 Test Configuration

The dovetail pull tests were conducted at NASA Glenn Research Center Building 51 on an electromechanical load frame as shown in Figure 5.001.

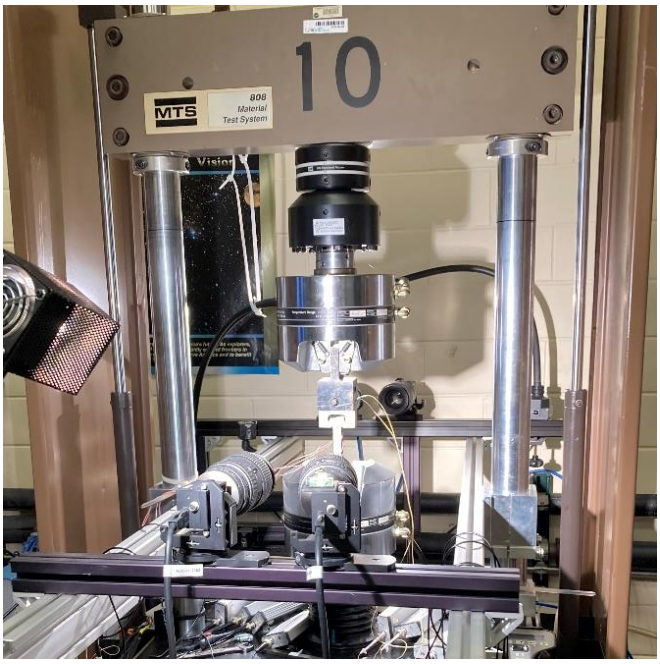

Figure 5.001: Dovetail pull test configuration with DIC.

The dovetail specimen is mounted in an inverted fashion with the dovetail secured in a fixture with a load-plate and set screw providing positive displacement to keep the dovetail specimen aligned and in-contact with the slot. The lower end of the specimen is gripped by the flat wedge grips with an aluminum mesh interface. DIC cameras are installed in-front of and behind the dovetail specimen to monitor both the forward and aft faces during the test. Additionally, acoustic emission sensors and strain gages are applied to the test specimen for monitoring during the test.

The test is run monotonically to failure using a displacement rate of approximately 3.337 E-4 in/sec. Testing is halted upon separation of the test specimen or a reduction in observed load.

5.2.4 Pre-test Predictions

The failure criterion are evaluated against legacy GE pull-test data for solid CMC blade pull-test articles. In prior experience GE observed interlaminar damage validated by audible emissions and strain measurements. The first major damage of the specimen was observed at an interlaminar stress of 16.8 ksi, and final failure at an interlaminar tensile stress of 18.14 ksi. A finite element model of the cooled blade dovetail pull-test specimen was constructed consisting of the assembly of the pull-test specimen and the fixture with the dovetail slot with surface-to-surface contact pairs (Figure 5.002).

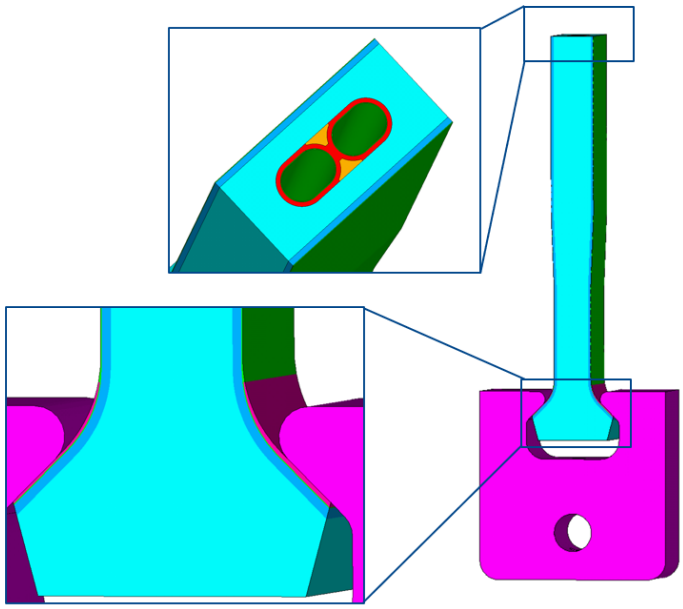

Figure 5.002: Dovetail specimen FEM model configuration and materials.

The model of the dovetail pull test specimen is fully partitioned by laminate definition and utilizes directionally dependent material properties. The material properties are aligned to the underlying laminate by using the ply surfaces to orient the element co-ordinate systems. After initial set-up, the model is exercised in tension, with the clevis hole under the dovetail slot having a fixed displacement. A load of 15,000 lbf is then applied to the model, at the free end opposite of the dovetail. This matches the upper limit of calibration for the electromechanical load frame planned for the test. The plot shown below in Figure 5.003 is obtained from the static stress result showing the interlaminar stress at the limiting location in the dovetail test specimen.

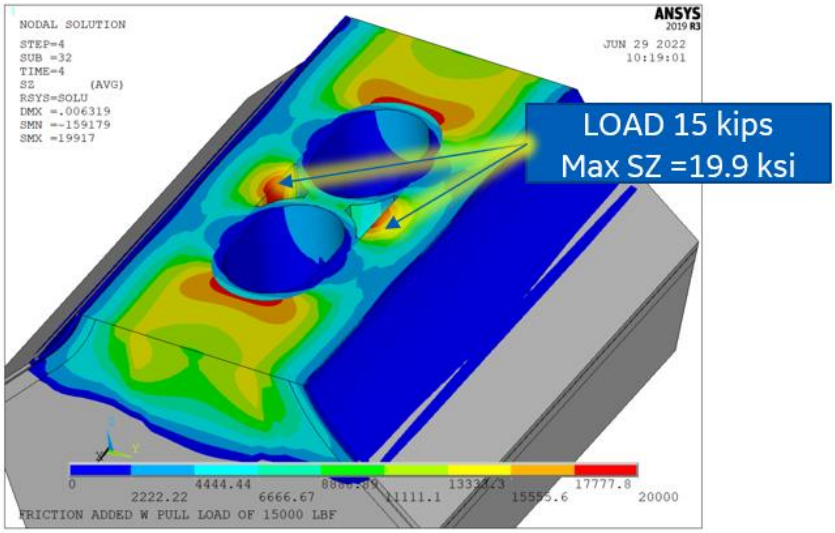

Figure 5.003: ILT Stress contour plot for 15,000 lbf load

By scaling the 19.9 ksi interlaminar stress to the legacy first audible stress of 16.8 ksi an expected first damage load of 12,663 lbf is obtained. Similarly, linearly scaling the 19.9 ksi interlaminar stress to the 18.14 ksi failure stress determines a final expected loading of 13,674 lbf for complete specimen failure.

5.2.5 Test Results

All eight test specimens were tested monotonically to failure with strain readings and load levels recorded. Figure 5.004 below shows the data collected for the dovetail monotonic pull tests; where blue indicates a specimen manufactured using a wet layup process while green indicates a specimen with a green machined cavity. The lighter color variant of the lot is intended to indicate the load at which the first evidence of damage was observed in the DIC images.

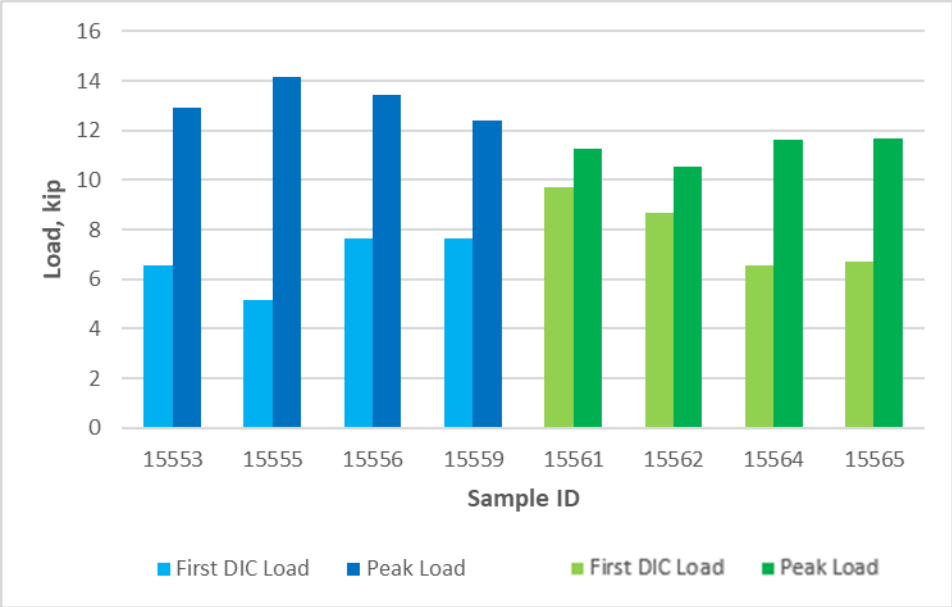

Figure 5.004: Initial damage and final failure load for the population of CMC dovetail pull-test articles tested and compiled by the NASA GRC test team.

The average first DIC indication across both sets is 7,338 lbf of load. The average peak load across the configurations is 12,245 lbf, but the wet layup population has a noticeably higher average max load of 13,219 lbf while the green machined population has an average peak load of 11,271 lbf. When comparing the ultimate failure load of the specimen the Wet Layup configuration compares favorably with the 13,674 lbf failure load prediction.

Qualitatively two different types of failures were observed. One failure type consisted of damage popping-in and then propagating to fail the dovetail pull test specimen in a symmetric manner as viewed in Figure 5.005.

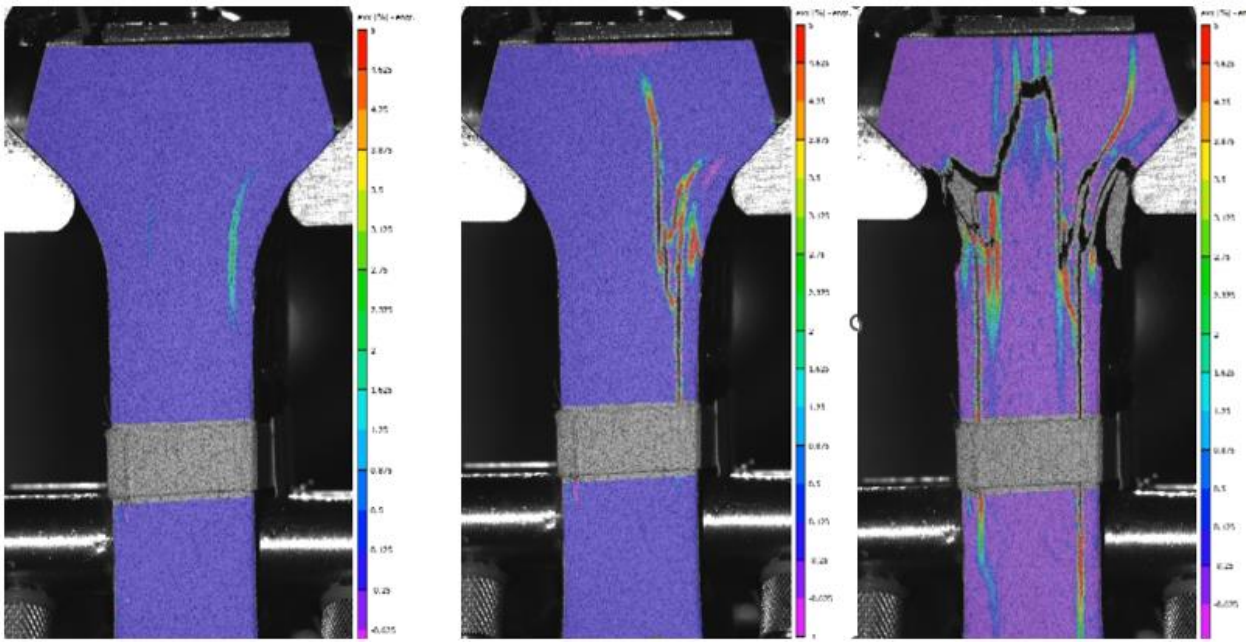

Figure 5.005: Specimen FW15555, Example of a symmetric failure progression where initiation occurs on one side of the dovetail, then propagates to a critical length, and finally connecting in a translaminar fashion to fail across the min neck of the specimen

The other type of failure observed is an asymmetric failure where damage propagates to a critical length and fails one side of the dovetail with the cooling passages isolating the other side as seen in Figure 5.006:

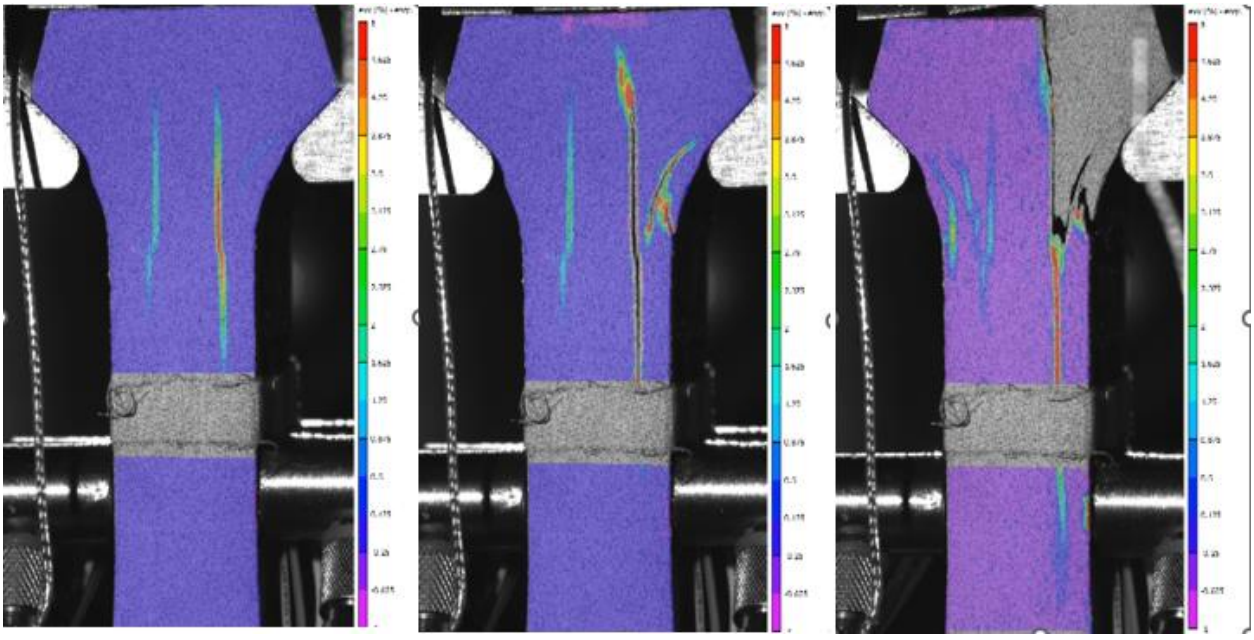

Figure 5.006: Specimen FW15553, Example of an asymmetric failure when damage propagates along one side of the shank prior to connecting the fillet radius and failing a single tang of the test article.

The interlaminar stress criterion (ILT) based on prior solid dovetail pull test specimen was accurate at predicting on a final failure basis, but did not accurately predict the initial damage observed in the DIC images. Possible explanations for this variation include small anomalies in the components or, a difference in load re-distribution between solid and cooled dovetail configurations. Within the cooled blade data set a different trend of initial damage versus load and final fracture versus load was observed when comparing the green machined specimens to the wet layup specimens.

5.3 Load Controlled HCF Test Program

5.3.1 Test Objective

The high cycle fatigue (HCF) test program conducted as part of the cooled blade development was created to further understand the impact of cooling holes oriented transversely to the primary loading direction. This testing is of value as turbine blades are cantilevered airfoils subject to vibratory loading induced by flow disturbances originating from upstream hardware and flow instabilities. The test parameters also reflect the turbine blade stress environment, primarily evident in the fatigue R-Ratio (the ratio of the minimum stress to the maximum stress in the fatigue cycle) and the specimen hole spacing. Learnings from this test campaign will provide additional data for feature driven HCF considerations and inform future efforts and procedures for assessing the interaction between transversely oriented cooling holes and vibratory loading.

5.3.2 Test Matrix

The load controlled HCF program is targeted to address vibratory stress concerns in airfoil critical locations. A total of 32 samples were utilized for the HCF testing, distributed across two different specimen configurations (baseline and hole drilled) as well as two temperature values (1500˚F and 2400˚F). The full test matrix is shown below in Table 5.002.

Table 5.002: Load Controlled HCF Test Matrix

Temp.	Config.	Test	Layup	R-Ratio	Material Lot	# of Specimens
1500F	Baseline	HCF	$m(0/90/0)_3m$	0.6	1	4
					2	4
	Kf	HCF	$m(0/90/0)_3m$	0.6	1	4
					2	4
2400F	Baseline	HCF	$m(0/90/0)_3m$	0.6	1	4
					2	4
	Kf	HCF	$m(0/90/0)_3m$	0.6	1	4
					2	4

One item of note in the test matrix is that the testing was conducted with an R-Ratio of 0.6. This test parameter was selected based on GE's prior experience with solid uncooled CMC blades and represents the presence of the airfoil mean stress resulting from the rotational loading of the turbine blade.

The design of the K_f specimen is intended to simulate the transversely oriented cooling holes utilized in the airfoil. The geometry utilized incorporates a 0.026" diameter round holes drilled at a 20-degree angle relative to the surface and are manufactured by an electrical discharge machining process (EDM). There are a total of five holes present on the specimen with a hole spacing of seven diameters measured from the hole center; hole count was limited by the gage length of the specimen. Figure 5.007 depicts the nominal model of the cooling hole specimen as well as an image of an as-manufactured specimen.

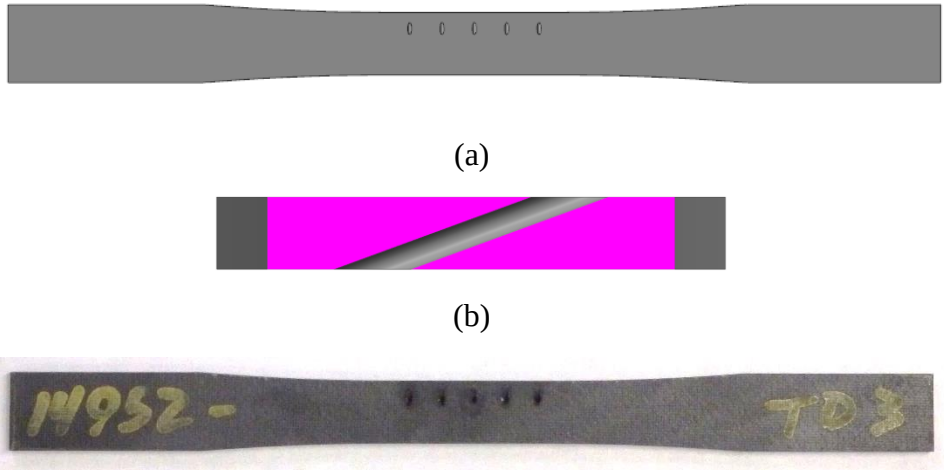

(a)

(b)

(c)

Figure 5.007: (a) Nominal specimen model with simulated cooling holes (b) Cross-section view depicting simulated cooling hole placement (c) As-manufactured test specimen

5.3.3 Test Results Summary

The entirety of the HCF testing campaign was performed at the NASA Glenn Research Center by NASA and HX5 personnel (ref. 2). Table 5.003 and Table 5.004 present the tabulated test results; test parameters are presented in the upper portion of the tables. The first half of each table corresponds to the baseline test specimen (no simulated cooling holes); while the second half of the data tables correspond to the specimen that contained simulated cooling holes.

Table 5.003: 1500F Load Controlled HCF Summary

Control Mode : Load
Dynamic Ratio : R = 0.60
Test Temperature : 1500°F

Frequency : 30 Hz
Waveform : Sinusoidal
Removal Point : 30,000,000

Specimen Number	Width (in)	Thickness (in)	R-Ratio	Max. Stress (ksi)	Max Load (lbf)	Mean Load (lbf)	Alt. Load (lbf)	Min. Load (lbf)	Cycles	Results	Test Hours
14946-TD-2	0.4017	0.0775	0.60	44.0	1369.8	1095.8	274.0	821.9	5,088,000	Failure	47.1
14946-TD-4	0.4012	0.0779	0.60	46.0	1437.7	1150.1	287.5	862.6	2,049,400	Failure	19.0
14947-TD-1	0.4013	0.0775	0.60	48.0	1492.8	1194.3	298.6	895.7	3,083,041	Failure	28.5
14947-TD-3	0.4019	0.0778	0.60	35.0	1094.4	875.5	218.9	656.6	30,000,000	Removal	277.8
14950-TD-1	0.4005	0.0798	0.60	52.0	1661.9	1329.5	332.4	997.1	459,065	Failure	4.3
14950-TD-3	0.4009	0.0798	0.60	38.0	1215.7	972.6	243.1	729.4	4,296,061	Failure	39.8
14951-TD-2	0.4011	0.0798	0.60	41.0	1312.3	1049.9	262.5	787.4	3,608,910	Failure	33.4
14951-TD-4	0.4012	0.0795	0.60	36.0	1148.2	918.6	229.6	688.9	30,000,000	Removal	277.8
14948-TD-3	0.4007	0.0772	0.60	30.0	928.0	742.4	185.6	556.8	16,391,824	Failure	151.8
14948-TD-5	0.4004	0.0770	0.60	40.0	1233.2	986.6	246.6	739.9	181,404	Failure	1.7
14949-TD-2	0.4006	0.0766	0.60	35.0	1074.0	859.2	214.8	644.4	679,371	Failure	6.3
14949-TD-4	0.4006	0.0777	0.60	32.0	996.1	796.8	199.2	597.6	7,843,063	Failure	72.6
14952-TD-2	0.4013	0.0796	0.60	31.0	990.2	792.2	198.0	594.1	9,715,279	Failure	90.0
14952-TD-4	0.4013	0.0794	0.60	33.0	1051.5	841.2	210.3	630.9	785,401	Failure	7.3
14953-TD-1	0.4009	0.0790	0.60	28.0	886.8	709.4	177.4	532.1	30,000,000	Removal	277.8
14953-TD-3	0.4015	0.0790	0.60	30.0	951.6	761.2	190.3	570.9	11,994,411	Failure	111.1

Table 5.004: 2400F Load Controlled HCF Summary

Control Mode : Load
Dynamic Ratio : R = 0.60
Test Temperature : 2400°F

Frequency : 30 Hz
Waveform : Sinusoidal
Removal Point : 30,000,000

Specimen Number	Width (in)	Thickness (in)	R-Ratio	Max. Stress (ksi)	Max Load (lbf)	Mean Load (lbf)	Alt. Load (lbf)	Min. Load (lbf)	Cycles	Results	Test Hours
14946-TD-1	0.4016	0.0782	0.60	31.0	973.6	778.8	194.7	584.1	30,000,000	Step Load	277.8
14946-TD-1 (SL)	0.4016	0.0782	0.60	40.0	1256.2	1005.0	251.2	753.7	9,956	Failure	0.1
14946-TD-3	0.4015	0.0776	0.60	38.0	1183.9	947.2	236.8	710.4	647,574	Failure	6.0
14947-TD-2	0.4016	0.0772	0.60	36.0	1116.1	892.9	223.2	669.7	9,777,044	Failure	90.5
14947-TD-4	0.4020	0.0784	0.60	34.0	1071.6	857.3	214.3	642.9	30,000,000	Removal	277.8
14950-TD-2	0.4010	0.0797	0.60	39.0	1246.4	997.1	249.3	747.9	133,635	Failure	1.2
14950-TD-4	0.4011	0.0799	0.60	37.0	1185.8	948.6	237.2	711.5	126,390	Failure	1.2
14951-TD-1	0.4009	0.0795	0.60	35.0	1115.5	892.4	223.1	669.3	19,323,665	Failure	178.9
14951-TD-3	0.4014	0.0800	0.60	36.0	1156.0	924.8	231.2	693.6	511,835	Failure	4.7
14948-TD-1	0.4006	0.0768	0.60	26.0	799.9	639.9	160.0	480.0	669,040	Failure	6.2
14948-TD-4	0.4004	0.0773	0.60	22.0	680.9	544.7	136.2	408.6	27,842,390	Failure	257.8
14949-TD-3	0.4003	0.0765	0.60	25.0	765.6	612.5	153.1	459.3	11,942,477	Failure	110.6
14949-TD-5	0.4008	0.0769	0.60	27.0	832.2	665.7	166.4	499.3	967,641	Failure	9.0
14952-TD-1	0.4014	0.0796	0.60	28.0	894.6	715.7	178.9	536.8	210,980	Failure	2.0
14952-TD-3	0.4012	0.0793	0.60	26.0	827.2	661.8	165.4	496.3	1,176,128	Failure	10.9
14953-TD-2	0.4012	0.0791	0.60	23.0	729.9	583.9	146.0	437.9	30,000,000	Removal	277.8
14953-TD-4	0.4018	0.0791	0.60	24.0	762.8	610.2	152.6	457.7	1,886,479	Failure	17.5

Figure 5.008 below from the HX5 and NASA test report shows the combined S-N curves of the baseline and cooling hole 1500°F specimens.

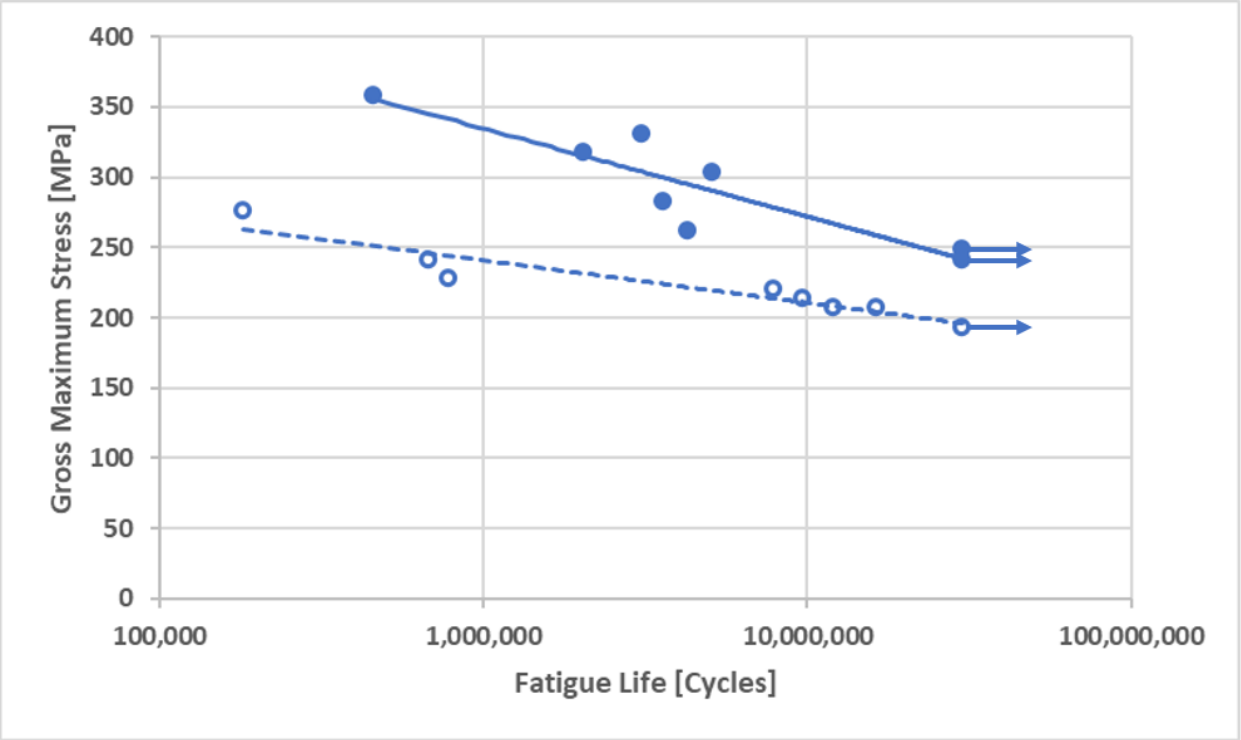

Figure 5.008: HX5 & NASA test report plotting gross stress vs. cyclic life for 1500°F baseline (filled in circles) and cooling hole specimen (open circles) [reference 2]

The plotted S-N curves for the 1500°F tests depict a reduction in HCF capability when analyzed on a gross stress basis (i.e. not accounting for the reduction in cross-sectional area from the cooling holes). The HX5 and NASA team also assessed to impact of the cooling holes relative to net-section stresses in the sample; this data is plotted in Figure 5.009 below.

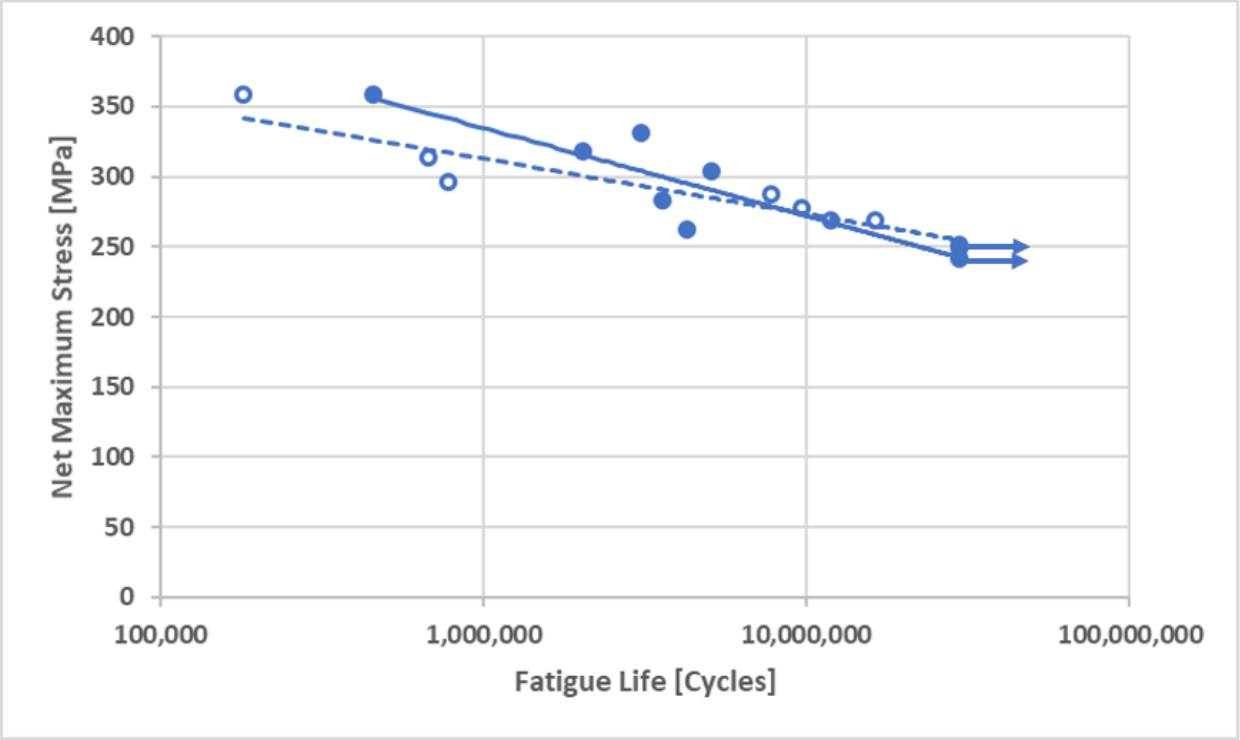

Figure 5.009: HX5 & NASA test report plotting net-section stress vs. cyclic life for 1500°F baseline (filled in circles) and cooling hole specimen (open circles) [reference 2]

With the correction made for the material missing from the hole drilling process the cooling hole specimen data the fatigue lives more closely match the baseline test specimen, albeit with a slight change in slope of the fitted data points due to lower cycle failures in the cooling hole specimens at high stress levels. Similar results are also shown below for the 2400°F test data on a gross stress (Figure 5.010) and net-section stress (Figure 5.011) basis.

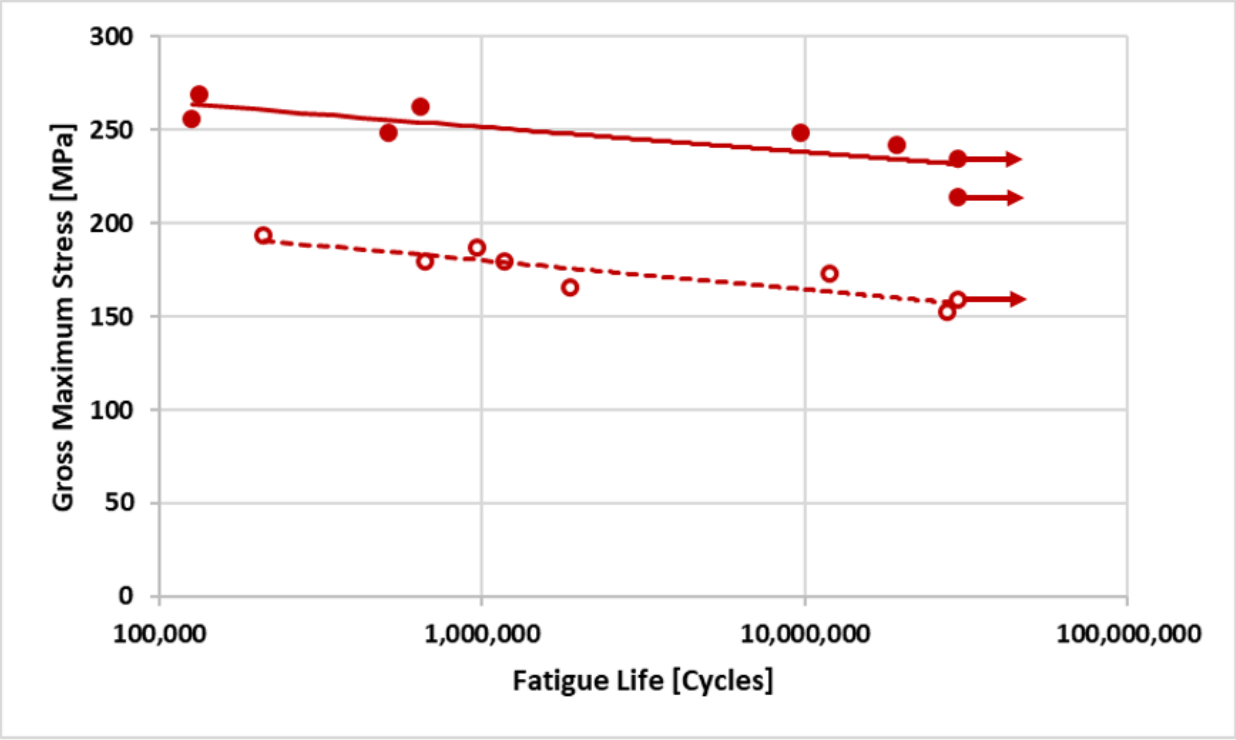

Figure 5.010: HX5 & NASA test report plotting gross stress vs. cyclic life for 2400°F baseline (filled in circles) and cooling hole specimen (open circles) [reference 2]

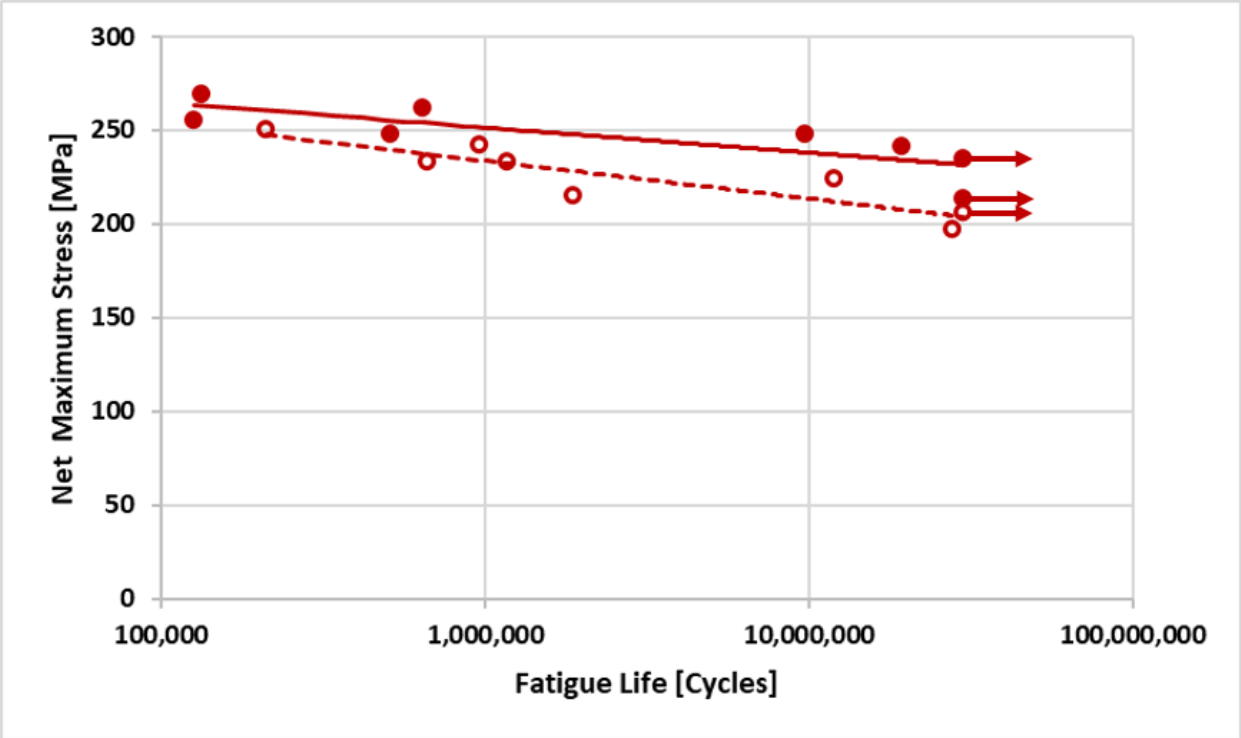

Figure 5.011: HX5 & NASA test report plotting net-section stress vs. cyclic life for 2400°F baseline (filled in circles) and cooling hole specimen (open circles) [reference 2]

In the 2400°F gross stress data, a clearly distinguishable delta can be seen between the baseline and cooling hole specimen data, which is similar to observations made in the 1500°F testing. When the data is adjusted on a net-section stress basis to account for the reduction in cross-sectional area due to the presence of the cooling holes the cooling hole data adjusts upward, but does not fully collapse onto the baseline specimen data. This would indicate that there is an impact on high cycle fatigue capability due to the presence of the cooling holes.

5.3.4 Load Controlled HCF Summary

The material testing in this effort will serve to expand the available database of HCF information to substantiate the design space for cooled CMC components. For the cooled CMC blade test article, cooling holes were not explicitly modeled in the finite element model for the cooled CMC blade test article. Also, no adjustment was made to material stiffnesses to account for the holes. It is recommended that the knockdown factors based on gross stress be used for this method of analysis.

5.4 Strain Controlled SPLCF (eSPLCF) Program

5.4.1 Test Objective

The objective of the strain controlled sustained peak low cycle fatigue (eSPLCF) program is to determine the impact of transverse cooling holes with respect to eSPLCF durability. This testing is of value for locations within the blade that contain thermally dominated strain/stress states. An example for the cooled CMC Blade test article is the aft cavity region where many of the transverse cooling holes intersect the cavity. This region receives an appreciable amount of bore cooling due to the high concentration of cooling holes feeding from the aft cavity. Due to the high gas path temperatures relative to the cooling air temperature this results in a thermal gradient induced strain in the region where the cooling holes are present.

5.4.2 Test Matrix

The eSPLCF testing is a long duration test relative to an HCF test; a target removal point of 20,000 cycles can result in a test duration of roughly 678 hours due to a 2-minute hold time in the testing waveform. The long test durations and material availability constraints placed some practical limitations on the size of the test matrix. The test campaign consisted of sixteen samples as shown in Table 5.005 shown below.

Table 5.005: eSPLCF Test Matrix

Temp.	Config.	Test	Layup	R-Ratio	Material Lot	# of Specimens
1500F	Baseline	eSPLCF	$m(0/90/0)_3m$	0	1	4
					2	4
	Kf	eSPLCF	$m(0/90/0)_3m$	0	1	4
					2	4

Specimens were tested in two configurations, a baseline CMC specimen and a specimen with EDM drilled cooling holes consistent with the HCF test program as shown in Figure 5.007 in the prior section of this report. Each configuration included panels made from different raw material lots. The test was carried out at a R-Ratio equal to 0 to isolate the impact of the thermal cycling on specimen configuration durability. A temperature of 1500°F was selected to represent critical strain-controlled locations in the cooling passage surface as compared to the flowpath surface. These cold regions are driven into a tensile stress state as the hotter neighboring material expands due to thermal growth. Strain levels for the testing were selected as testing proceeds to populate points along an estimated total strain-life curve. All testing was conducted at GE's materials behavior facility in Evendale, Ohio.

5.4.3 Test Results

Table 5.006 shows the tabulated results from the eSPLCF testing which are also plotted in Figure 5.012 below. The first half of the table corresponds to the baseline specimen (no cooling holes), while the second half of the table corresponds to the test specimen that contain simulated cooling holes.

Table 5.006 – 1500°F eSPLCF test results

Specimen Number	Width (in)	Thickness (in)	R-Ratio	Max. Strain (%)	Min Strain (%)	Cycles	Results	Test Hours	Test Machine
15317-TD2a	0.4013	0.0791	0.0	0.120	0.0	4,978	Stepped 0.14%	168.7	1008
15317-TD2b	0.4013	0.0791	0.0	0.140	0.0	0	FOL at 0.101%	0	1008
15318-TD3	0.4012	0.0781	0.0	0.125	0.0	1,354	Failure	45.9	1008
15319-TD4	0.4014	0.0786	0.0	0.122	0.0	1,979	Failure	67.1	1006
15319-TD2	0.4015	0.0787	0.0	0.118	0.0	18,319	Failure	620.8	1006
15320-TD4	0.4019	0.0763	0.0	0.110	0.0	22,491	Removal	762.2	1006
15321-TD2	0.4019	0.0763	0.0	0.130	0.0	1,673	Failure	56.7	1008
15322-TD3	0.4018	0.0766	0.0	0.120	0.0	21,165	Removal	717.3	1008
15322-TD5	0.4013	0.0761	0.0	0.124	0.0	2,990	Failure	101.3	1006
15317-TD3	0.4009	0.0787	0.0	0.130	0.0	197	Failure	6.7	1006
15317-TD4	0.4008	0.0797	0.0	0.090	0.0	2,415	Failure	81.8	1006
15318-TD4	0.4015	0.0794	0.0	0.125	0.0	586	Failure	19.9	1006
15319-TD1	0.4018	0.0789	0.0	0.122	0.0	358	Failure	12.1	1005
15320-TD2	0.4016	0.0769	0.0	0.117	0.0	844	Failure	28.6	1005
15320-TD5	0.4017	0.0772	0.0	0.112	0.0	381	Failure	12.9	1005
15321-TD4	0.4020	0.0772	0.0	0.105	0.0	950	Failure	32.2	1005
15322-TD1	0.4017	0.0769	0.0	0.097	0.0	2,010	Failure	68.1	1006

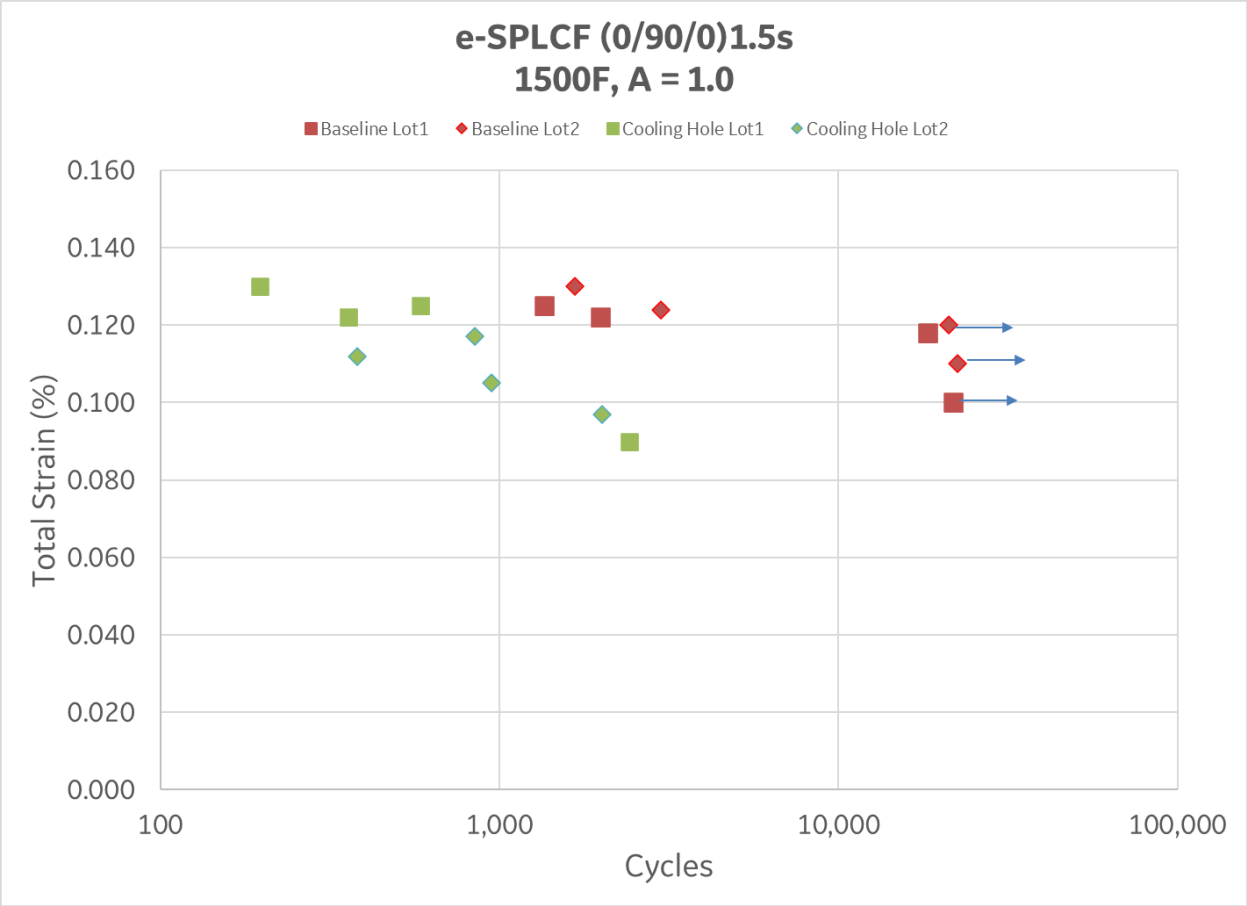

Figure 5.012: 1500°F eSPLCF testing for baseline and cooling hole specimen (arrows indicate run-out condition)

The data in Figure 5.012 shows that the cooling hole specimens have a lower eSPLCF capability than the baseline test specimens. It should be noted that no cooling hole specimen reached the removal point of 20,000 cycles during the test. As the removal point was not reached it is difficult to generate an appropriate K_f factor without the ability to generate a strain-life curve for the cooling hole data. With the available data from the test campaign, it does appear that the test specimens containing the cooling holes may exhibit a reduction in eSPLCF capability based on the limited overlap in the data points generated during testing. It is highly recommended that further testing be pursued to generate a complete total strain-life curve to determine an appropriate knockdown factor.

5.4.4 eSPLCF Summary

The testing campaign of the eSPLCF test specimens was tailored to the cooled CMC blade test article designed in this effort. For different cooling architectures and engine relevant hot gas path conditions different testing parameters may be of interest. This testing further informs the understanding of the impact that the cooling holes have on the limiting locations present within

the airfoil cavity with the cooling hole configuration expected to be used on the cooled CMC Blade test article. For further development and maturation of cooled CMC Blade technology, it is recommended that further testing be performed to fully account for the given component's design and operational parameters (hole spacing, surface angle, material temperature, etc.).

5.5 EBC Testing Program

5.5.1 Test Objectives

The CMC blade test article utilizes a state-of-the-art slurry based EBC system. This EBC system was matured at private expense through prior applications on cooled static turbine airfoils. For consideration for use on a cooled high pressure turbine CMC blade, experiments were conducted to evaluate the response of the existing EBC system with respect to impact [resulting from foreign object debris (FOD) or domestic object damage (DOD)] and solid particle erosion. Both tests were conducted at the NASA Glenn Research Center with collaboration from GE in determining the appropriate test parameters and test matrices.

5.5.2 Solid Particle Erosion Configuration and Test Matrix

The solid particle erosion testing was conducted at the NASA Glenn Research Center at the erosion test facility utilizing a modified Mach 0.3 Burner Rig as shown below in Figure 5.013.

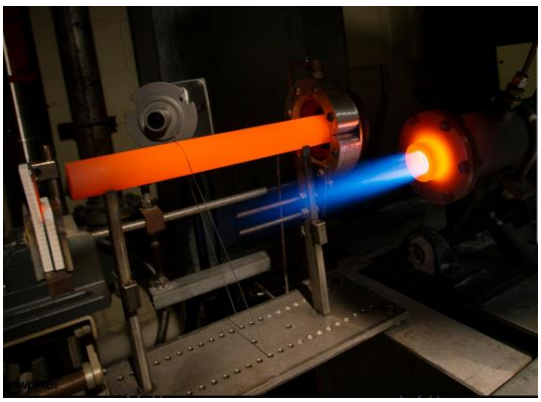

Figure 5.013: NASA Glenn Solid Particle Erosion Facility

In this rig, one inch diameter EBC coated CMC button specimens are placed downstream of movable duct at a pre-determined impingement angle. For testing, erosion media (Al_2O_3 particulate) is introduced into the burner combustion chamber and accelerated though the duct toward the CMC button specimen. The test assessed multiple configurations of particle size, particle velocity and impingement angle. The comprehensive test matrix is displayed below in Table 5.007.

Table 5.007: High Temperature Erosion Test Matrix

Test Condition	Sample Definition	Temperature (°C)	Particle Chemistry	Erodent Velocity (m/s)	Particle Size (micron)	Impingement Angle (°)	# of Specimens
1	1" button	1200	Al_2O_3	100	60	30	3
						90	3
2	1" button	1200	Al_2O_3	100	150	30	3
						90	3
3	1" button	1200	Al_2O_3	135	60	30	3
						90	3
4	1" button	1200	Al_2O_3	135	150	30	3
						90	3

5.5.3 Solid Particle Erosion Results Summary

Prior to testing and post test, each specimen was weighed to determine the cumulative mass lost during testing. The results post-processed by the NASA Glenn team are shown below in Figure 5.014 for the 60-micron particulates and Figure 5.015 for the 150-micron particulates.

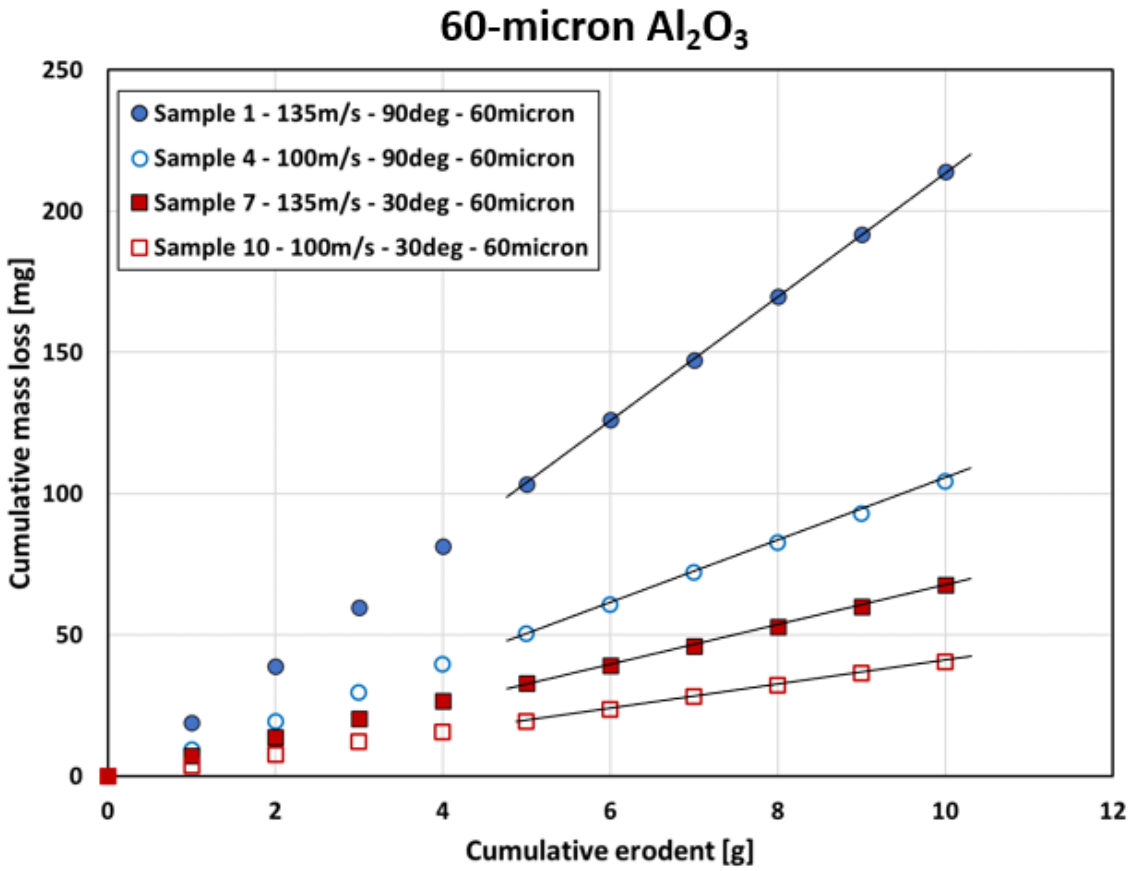

Figure 5.014: 60-micron cumulative mass loss vs. cumulative particulate erodent

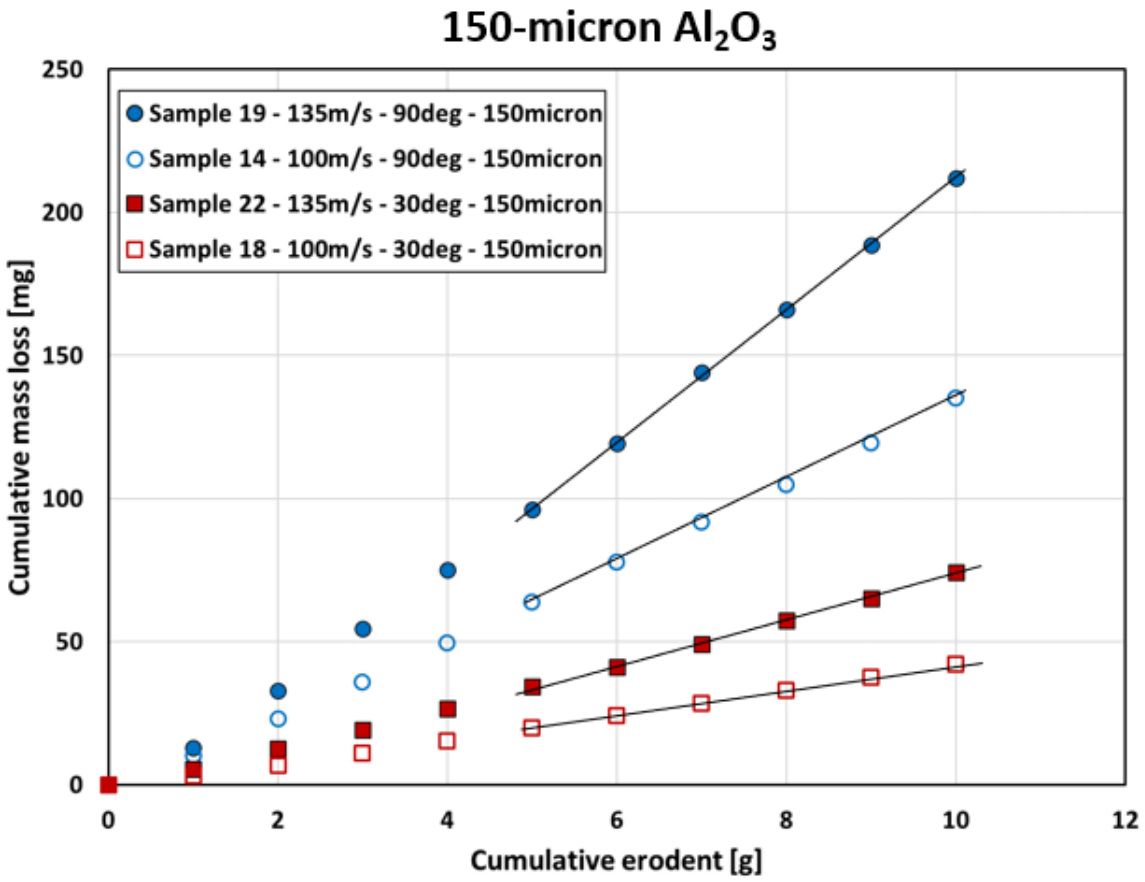

Figure 5.015: 150-micron cumulative mass loss vs. cumulative particulate erodent

The specimen mass loss trended positively with the particulate velocity and incidence angle (increasing incidence angle approaching vertical), while the cumulative mass loss with respect to particulate diameter, with other variables held constant, were similar across both particulate sizes utilized in testing. Relative to the needs of the CMC blade test article, these findings identify key parameters influencing the solid particle erosion capability of the EBC system.

5.5.4 Ballistic Impact Configuration and Test Matrix

Ballistic impact testing was also conducted at NASA Glenn research center, where a total of 4 specimens were tested at room temperature conditions with spherical stainless-steel impactors. The complete test matrix is shown below in Table 5.008.

Table: 5.008: Ballistic Impact Test Matrix

Test Condition	Sample Definition	CMC Config.	EBC Config. (mil)	Velocity (m/s)	Projectile (mm)	Temperature (°C)	# of Specimens
1	2" x 0.5"	8 ply	14	115	1.59	25	2
2	2" x 0.5"	8 ply	14	300	1.59	25	2

Differing from the erosion test specimens, the ballistic test specimens are 2 inches by 0.5 inch rectangular coated panels. This specimen size was specified by the NASA test facility and allows the panel to be partially supported across the span to simulate the compliance in the wall attributed to the cavity and rib configuration present in the cooled CMC blade architecture.

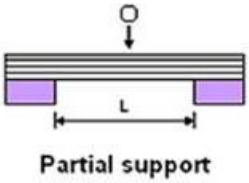

Figure 5.016: Specimen boundary condition arrangement

5.5.5 Ballistic Impact Results Summary

Of the four specimens tested, observations were similar between specimens in each impactor velocity group. The 115 m/s velocity tests showed minimal to minor cratering on the EBC side of the specimens with no backside damage observed on either specimen. Figure 5.017 below shows the worst-case damage observed in specimen GE-115-1 from the low-speed testing.

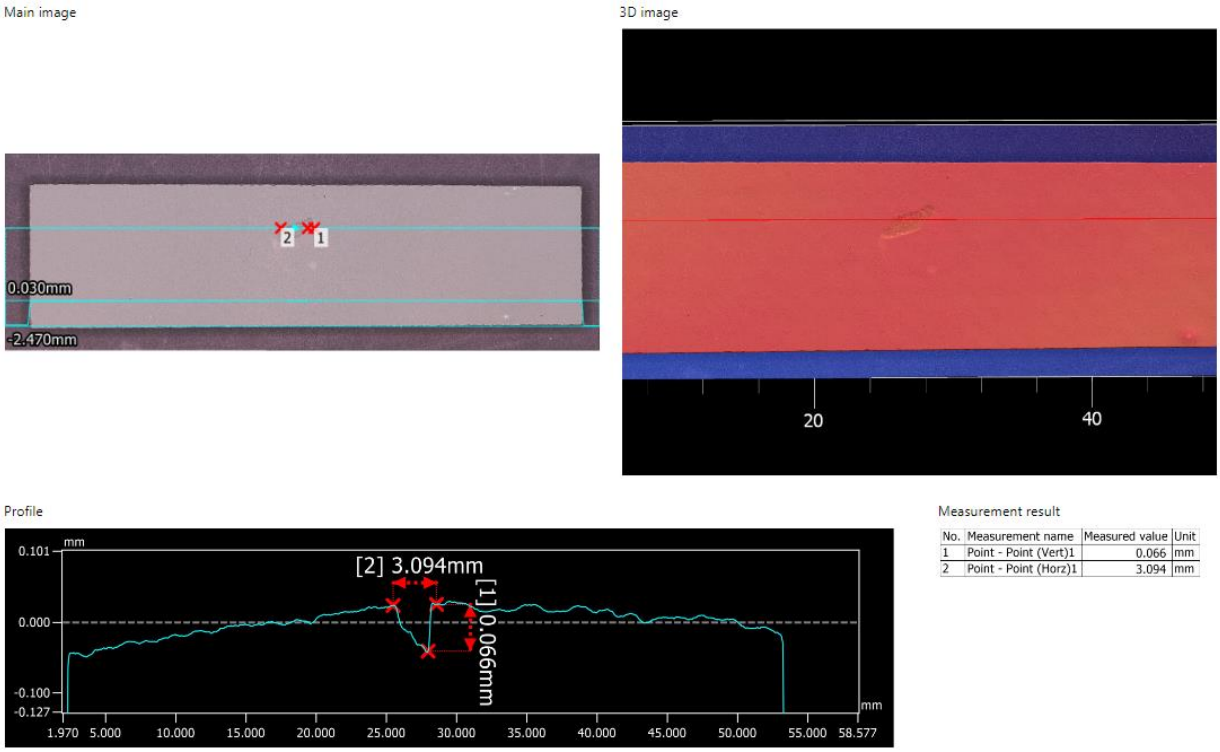

Figure 5.017: Specimen GE-115-1 front side images and profile trace depicting presence of small impact witness mark within EBC layer.

In the high speed (300 m/s) testing, both the depth and width of the visible damage on the EBC coated side of the specimen was increased relative to what was observed in the 115 m/s cases. Additionally, both 300 m/s test specimens exhibited the presence of backside (CMC) damage. Figure 5.018 shows the front side and back side distress of the first high speed impact test coupon, GE-300-1.

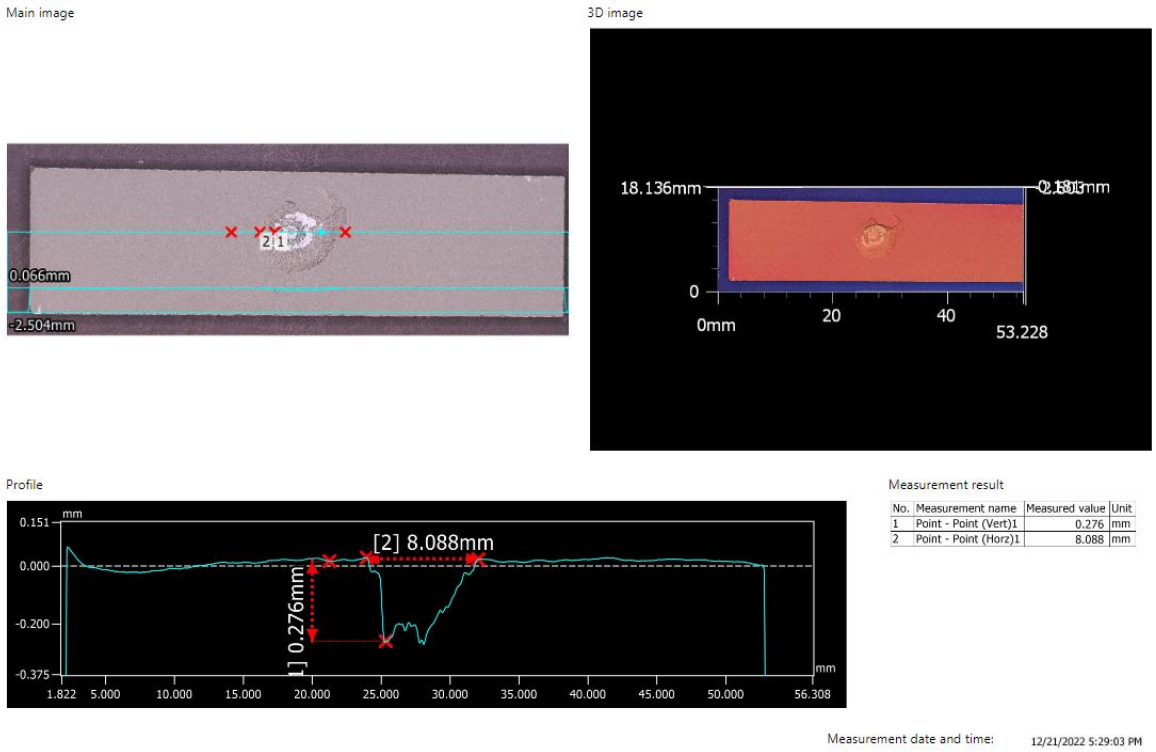

(a)

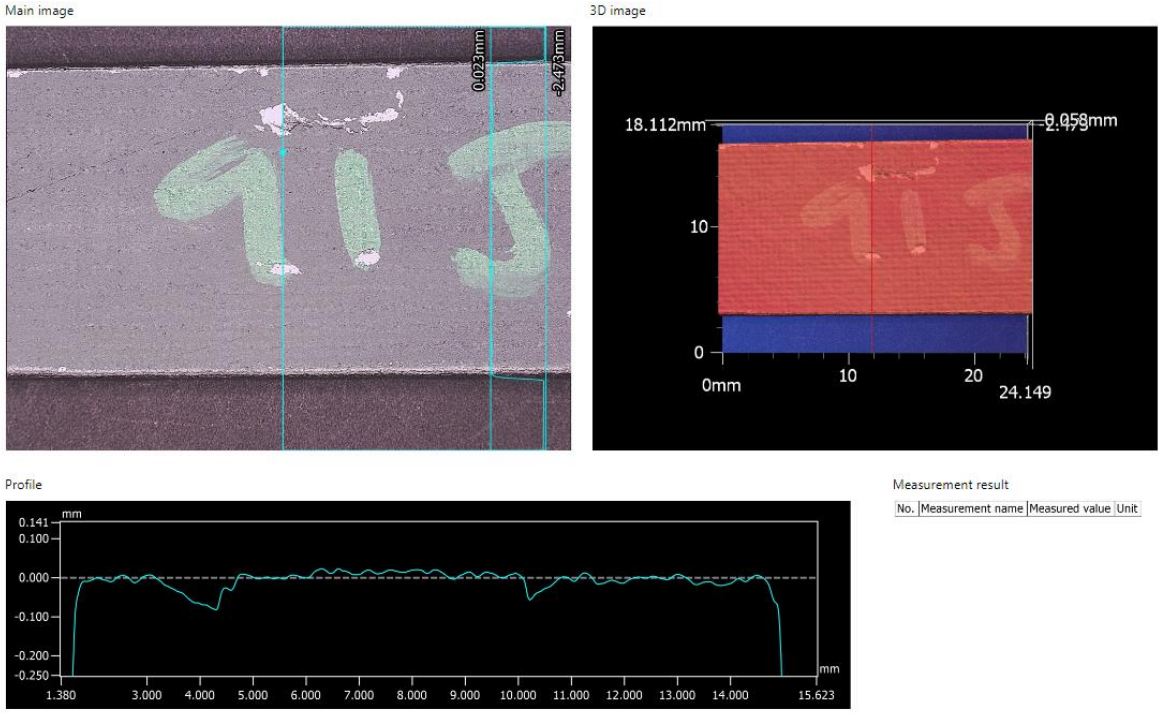

(b)

Figure 5.018: Post-test distress for specimen GE-300-1 depicting the coupon distress (a) front side of the specimen (b) back side of the specimen

The second high speed test specimen in Figure 5.019 below also exhibits the same broader impact crater as specimen GE-300-1

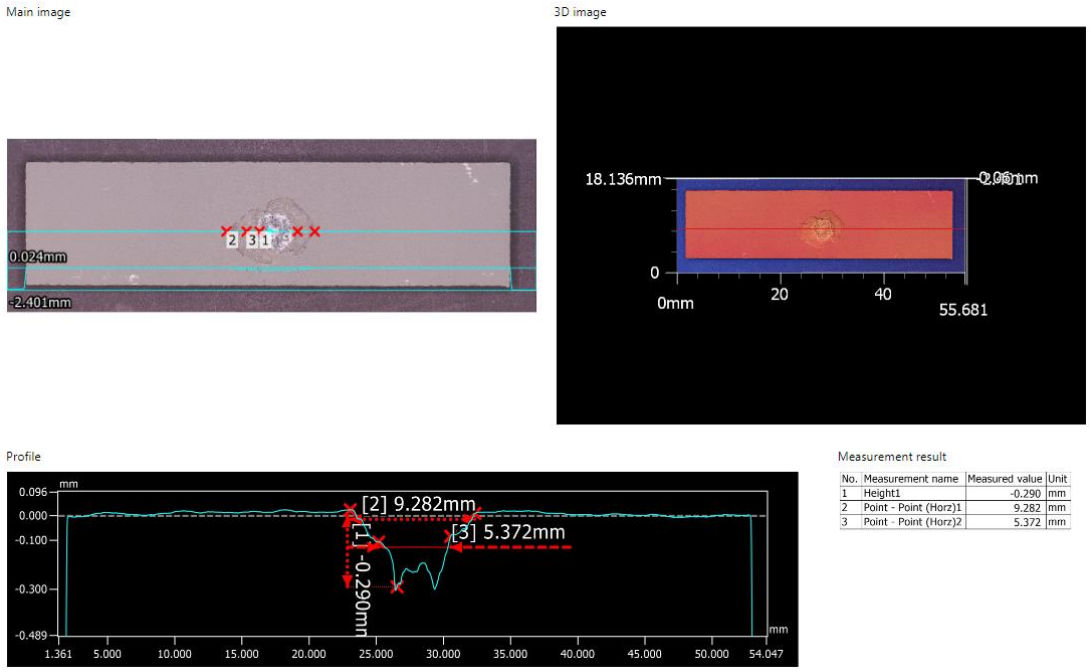

(a)

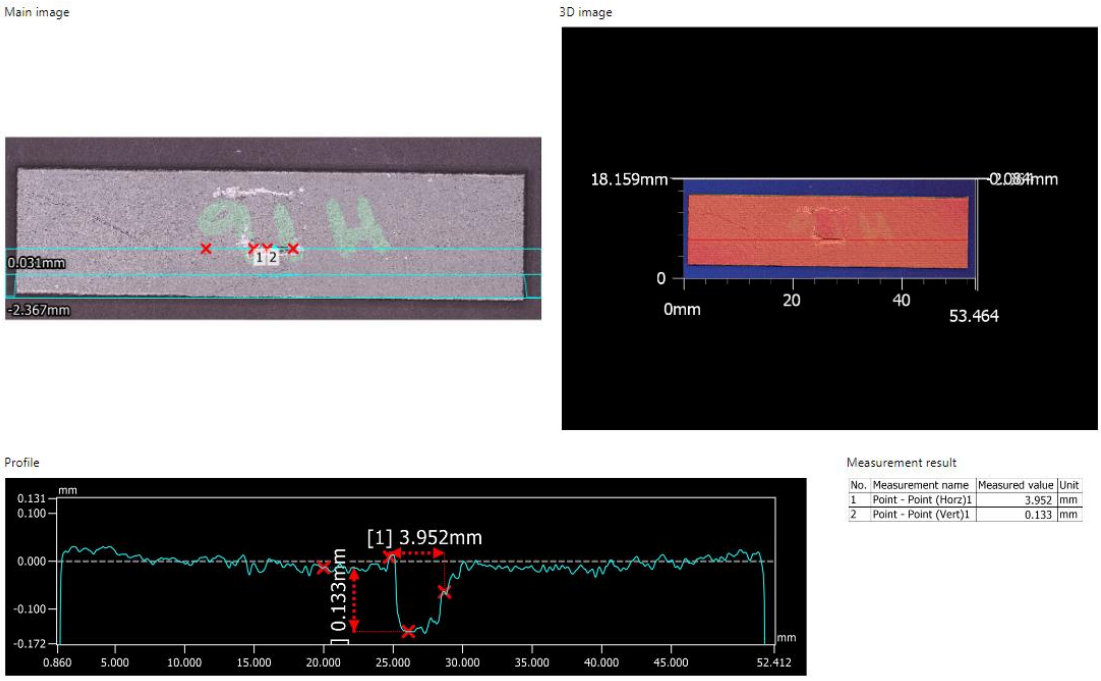

(b)

Figure 5.019: Post-test distress for specimen GE-300-2 depicting the coupon distress (a) front side of the specimen (b) back side of the specimen

5.5.6 EBC Testing Conclusions

Both the solid particle erosion testing and ballistic impact testing highlighted key distress modes for the slurry based EBC system utilized on the cooled CMC blade test article in a laboratory environment. These initial results will be foundational for any future efforts that expand upon how the baseline results scale across engine operating conditions of interest; informing design requirements for the CMC-EBC system to maintain the performance required of a high-pressure turbine blade.

6.0 Task 4 – Analysis

6.1 Summary

The objective of Task 4 was to model the baseline design of the CMC blade test article through Finite Element Analysis and apply acceptance criteria to predict failure modes and critical locations on the test article. As part of this effort the baseline cooled CMC blade test article was evaluated using ANSYS Finite Element Analysis software. The blade test article is further evaluated against GE's material database to determine design capability relative to a long-haul commercial turbofan durability requirement. Given that this is the first design effort to establish a baseline configuration of a cooled CMC blade, durability shortfalls will be predicted and a discussion of design abatements relative to critical design parameters and features will follow the analytical evaluation section to highlight a feasible path for improving durability margins.

6.2 General Analytical Approach

For the analysis of the baseline blade test article design and the dovetail sub-component test articles GE followed its standard approach for CMCs relative to stress analysis and lifing methodology. As part of this approach the appropriate material properties and durability curves from the GE materials database are used to assess the design with regards to the relevant failure modalities and material capability.

6.3 Blade Test Article Analysis

The analysis for the blade test article focused on the evaluation of the baseline blade design in engine relevant conditions. To accomplish this the blade test article is assessed at a steady state high power condition. Both the mechanical only (coefficient of thermal expansion = 0 to remove the strain contribution of thermal gradients) and total stress states (mechanical and thermal loading considered) were evaluated at this condition. Multiple iterations of the finite element model were

generated as the design matured through the development process, incorporating new geometric features. Early assessments of the test article also highlighted the need for increased mesh fidelity in critical locations.

6.3.1 Finite Element Model

The analysis approach for the blade test article utilized a bladed disk assembly model (Figure 6.001). This approach was selected over a blade only analysis to accurately represent the compliance of the system at the dovetail interface of the blade. A simplified high pressure turbine rotor, the design of which was not optimized for the NASA blade, which incorporated modified dovetail slot geometry to interface with the CMC dovetail was generated. Surface to surface contacts were used at the attachment interface between the blade pressure faces and the disk post pressure faces.

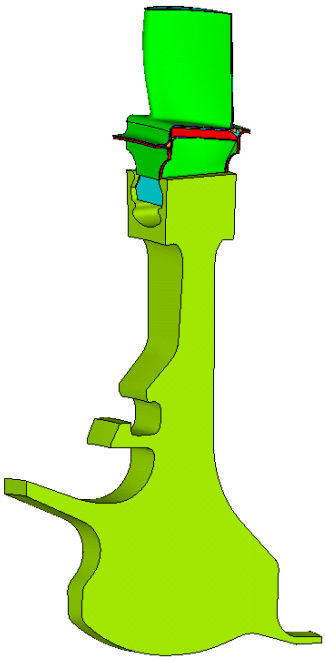

Figure 6.001: Bladed disk assembly analysis model

For the finite element model of the blade itself the mesh is partitioned to isolate regions of differing laminate architecture; appropriate laminate level orthotropic material properties are applied to each partitioned region (Figure 6.002).

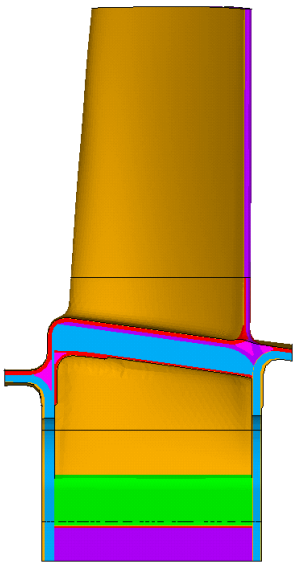

Figure 6.002: Profile view of the blade test article depicting various partitioned laminate regions indicated by model color variation

In addition to the partitioning of the model on a laminate basis, the element coordinate systems are aligned with the local fiber direction of the underlying laminate to properly model the orthotropic nature of the composite material. Temperatures and pressures are mapped to the blade model from a steady state thermal analysis at a high-power condition. The turbine disk leverages boundary conditions (temperatures, pressures, and displacements) from a prior mechanical assessment that was available for the that rotor.

6.3.2 Analysis Results

For the analysis of the blade test article several locations of interest were identified and evaluated relative to strain controlled SPLCF for the total stress state and load controlled SPLCF for the mechanical only stress state. These locations are documented below in Figure 6.003.

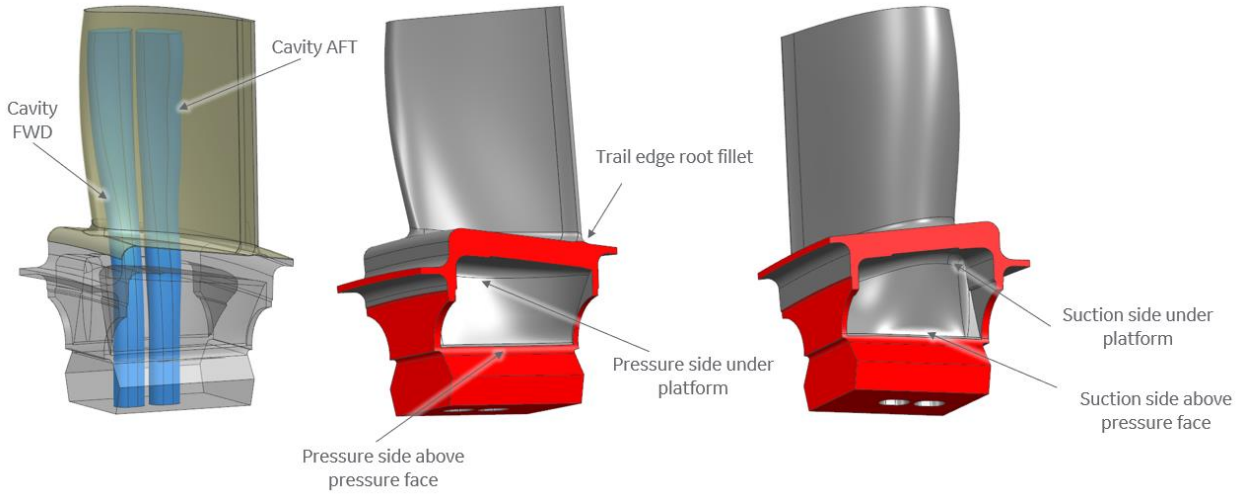

Figure 6.003: Identified regions of interest for limiting locations

6.3.2.1 Trail Edge Root Location

The first location reviewed on the blade was the trail edge root fillet location. Upon observing high local strain in the location, the local mesh fidelity and quality of the region was increased to accurately capture the stress state (Figure 6.004).

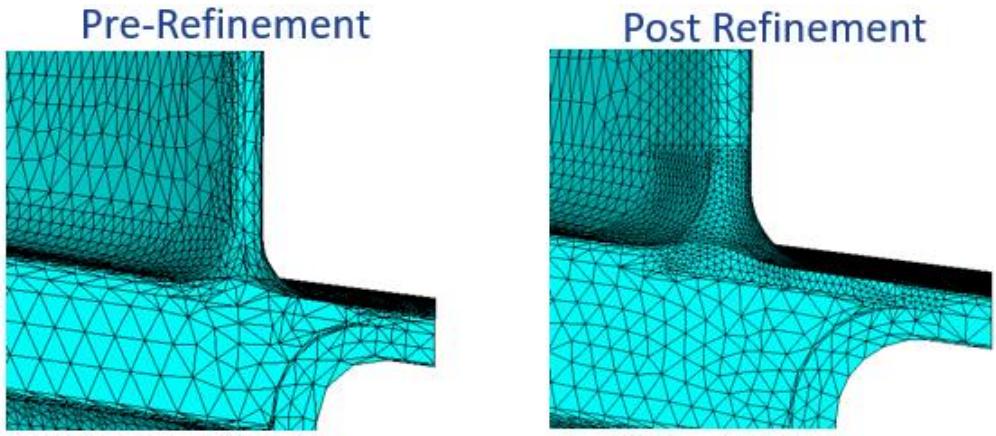

Figure 6.004: Images detailing the refinement of the trail edge root fillet location

Results from the total stress state show a very localized peak stress in the root fillet region of the trail edge of the airfoil. Areas of the trail edge of the airfoil located radially outboard of the root fillet exhibit relatively lower strain levels (Figure 6.005).

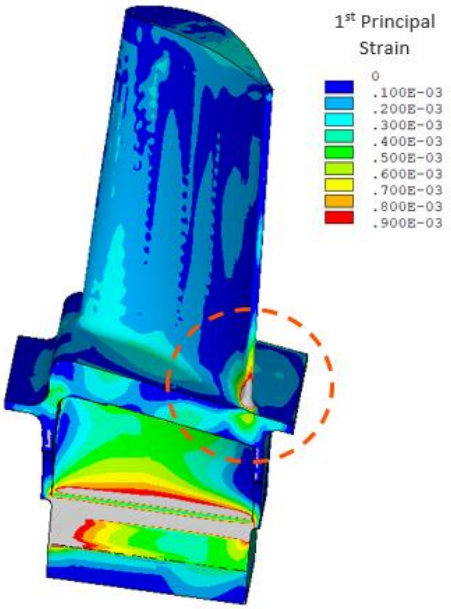

Figure 6.005: Contour plot of 1st principal strain detailing local strains at the trail edge root location for the total stress state

When evaluating against strain controlled SPLCF capability at the trail edge location there is a negative 44% strain margin relative to the material capability at that location. While outside of the scope of the program to redesign, discussions in section 6.3.3 will present options for improving life margin. When evaluating the mechanical only loading condition, a similar stress state was not observed at the trail edge root fillet feature (Figure 6.006).

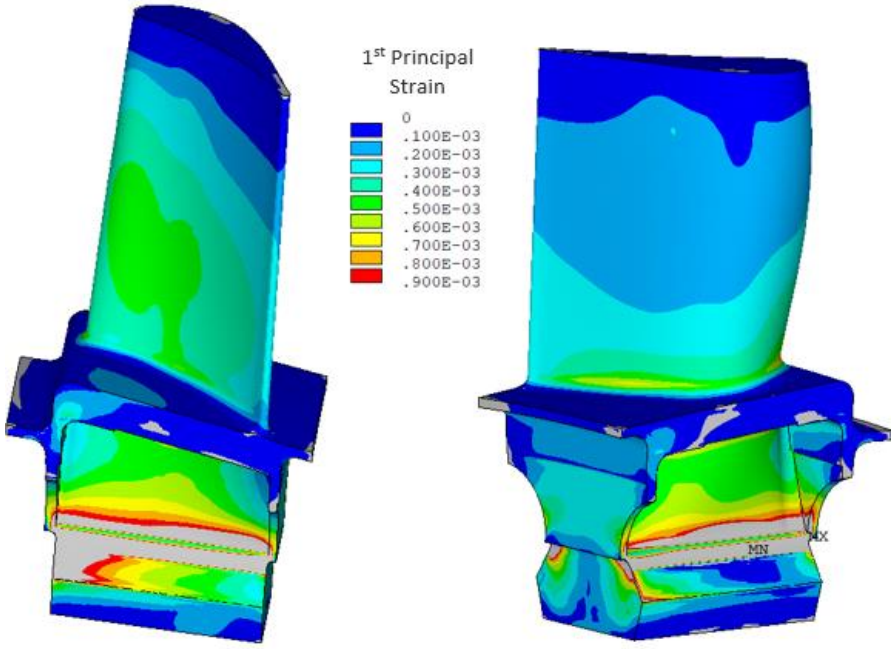

Figure 6.006: Contour plot of 1st principal strain for the mechanical only stress state

In the mechanical only finite element solution, the high stress region of the airfoil root fillet is biased towards the suction side panel of the airfoil relative to the trail edge. This indicates that the thermal gradient in the region is a significant contributor to the to the stress state at the trail edge.

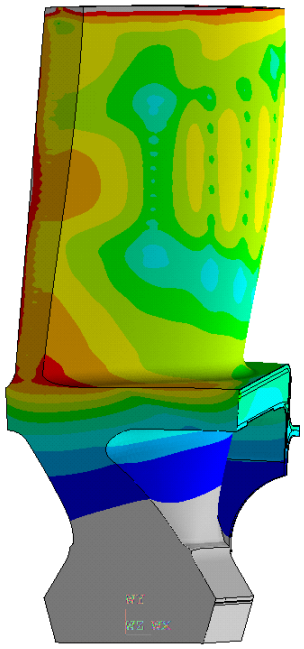

Figure 6.007: Thermal contour plot with axial plane truncation near the trail edge root fillet location

Upon inspection of the thermal state of the test article at an axial plane intersecting the location of interest as shown in Figure 6.007 a bulk temperature difference of approximately 700 degrees Fahrenheit was observed between the airfoil root and the blade shank which may influence the migration of strain from the suction side root fillet to the more highly concentrated location at the trail edge.

6.3.2.2 Under Platform Locations

The next family of locations of interest are the under-platform fillet regions of the test article depicted in Figure 6.008.

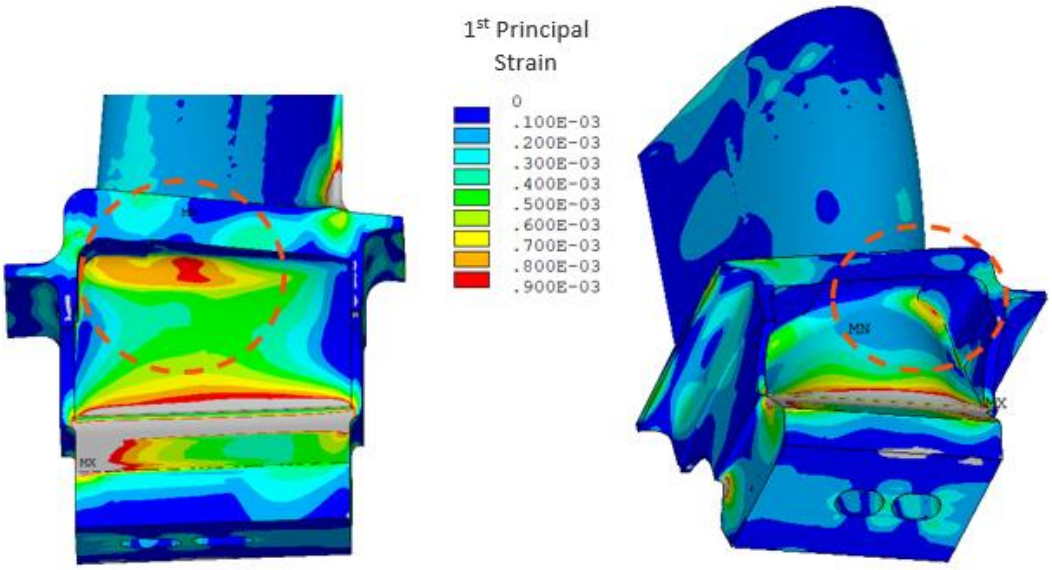

Figure 6.008: Contour plot of 1st principal strain detailing local strains at the under-platform locations evaluated using the total stress state

There is a location of high strain present on both the suction side and pressure side of the blade shank in the fillet radius beneath the blade platform. The pressure side location is near the rib between the cooling passages while the suction side limiting location is biased toward the forward cooling passage. Both locations meet strain controlled SPCLF targets with the pressure side location having a positive strain controlled SPLCF margin of 32% and the suction side location having a positive strain margin of 19%.

6.3.2.3 Shank Fillet Locations

The shank fillet locations located above the pressure faces of the dovetail attachment also exhibit high strain levels. Figure 6.009 details the strain contours for the shank region; it should be noted that strain results in the pressure face region of the dovetail attachment (highlighted with a red-bordered translucent box) located below the forward and aft skirt undercut are heavily influenced by the frictional contact and accurate stress calculation would require more detailed analysis techniques. It is anticipated that the cooling passage design will not have a significant adverse effect on these stresses, so these stresses were disregarded for the current evaluation. The region of primary region of interest is within the upper portion of the gray contour band.

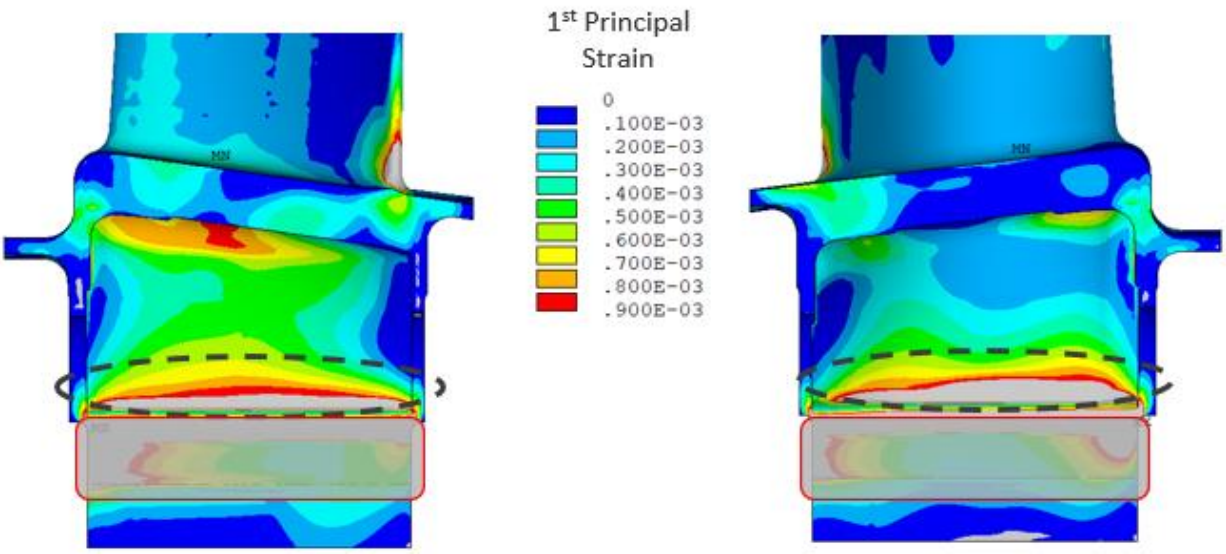

Figure 6.009: Contour plot of 1st principal strain detailing local strains at the shank fillet pressure side (left) and suction side (right) locations evaluated using the total stress state

Strains in this region are driven by the high inertial loading of the high-pressure turbine and the geometry constraints (the composite dovetail attachment must be packaged into the design space of the existing metallic configuration).

The radially biased laminate present on the surface of the shank has a negative 29.5% strain margin to meeting design targets while the suction side location has a negative 32.3% strain margin to meeting design targets. In the machining stock laminate present on the pressure face and the lower portion of the shank fillet, lower strain margins of negative 38.5% for the pressure side and negative 51% for the suction side were calculated.

6.3.2.4 Cavity Wrap Locations

The final locations of interest include the cavity wrap laminates in which high strain levels are calculated at locations where there is a high density of cooling holes intersecting the cavity. Figure 6.010 provides a strain contour distribution of the forward and aft cavities.

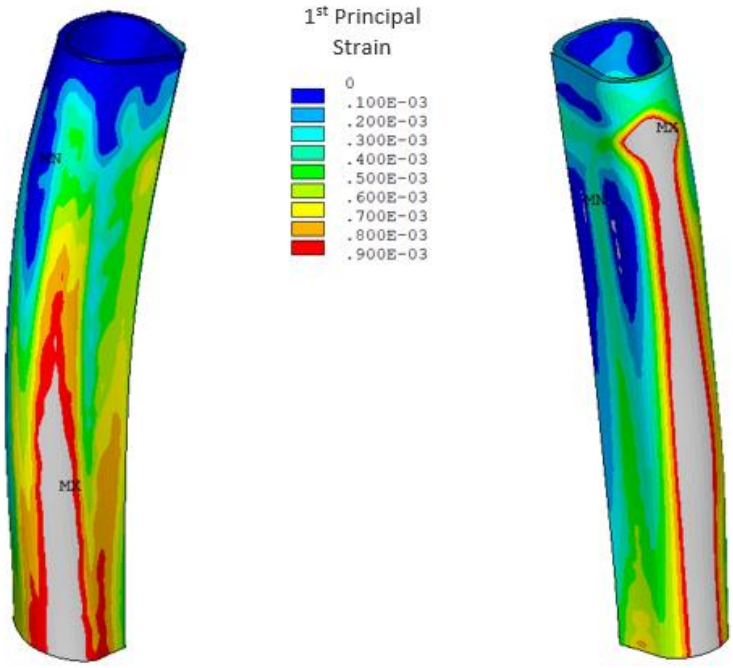

Figure 6.010: Contour plot of 1st principal strain detailing local strains at the lead edge of the forward cooling passage (left) and the trail edge of the aft cooling passage (right) for the total stress state.

The lower portion of the lead edge of the forward cavity is influenced by the thermal gradients from the concentration of cooling holes placed at the lead edge. The trail edge of the aft cavity also exhibits the same challenge as the rows of trail edge ejection cooling holes intersect the aft portion of the cavity driving, down temperature in the center of the blade (Figure 6.011).

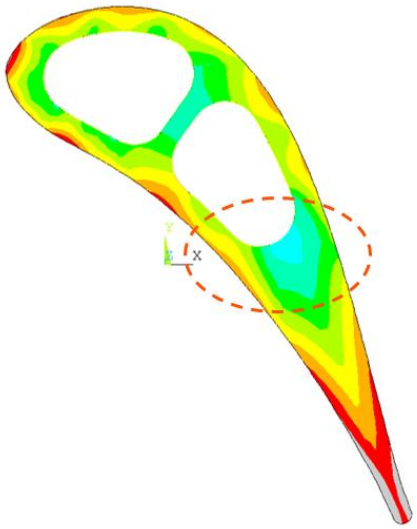

Figure 6.011: Mid-span temperature plot of the airfoil highlighting a cold region developed near the aft cooling passage

The region of the airfoil where the trail edge ejection cooling intersects the cooling passage supply develops an approximately 500-degree Fahrenheit temperature gradient from the center of the airfoil to the high temperature regions on the pressure side of the airfoil. This gradient drives a large tensile strain into the cold regions near the aft portion of the cavity. The resultant eSPLCF capability at the aft cavity is a negative 58.6% strain margin compared to the forward cavity which has a smaller thermal gradient resulting in a negative 48.2% strain margin.

6.3.3 Design Improvement Recommendations

6.3.3.1 Trail Edge Root Fillet

The high strain at the root fillet is likely driven by the bulk temperature difference between the airfoil root and the blade shank. The main contributor is that the CMC blade has a simplistic cooling circuit when compared to a traditional metallic high pressure turbine blade that would contain a serpentine passage and internal heat transfer coefficient enhancing features. This architectural difference increases the CMC blade design's reliance on film cooling to achieve an acceptable thermal state in the part. A derivative study was performed to assess the impact of additional targeted film cooling in the region.

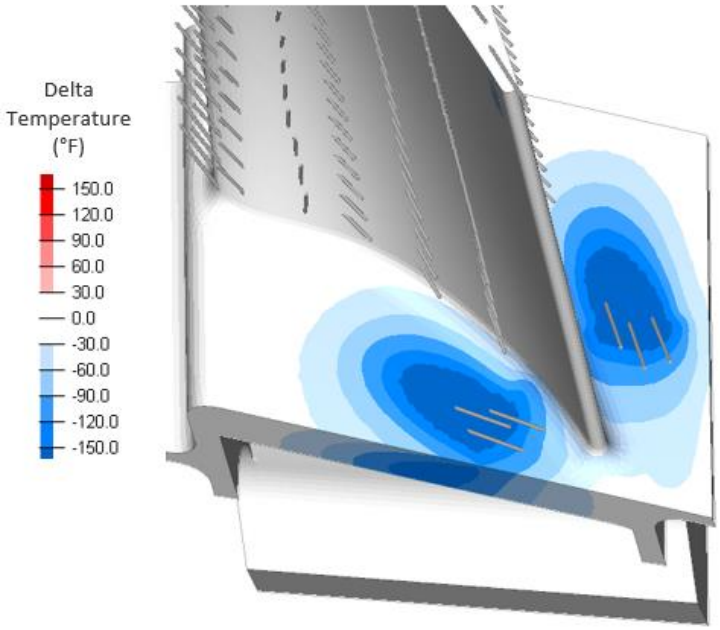

Figure 6.012: Contour plot of temperature change generated by introducing additional platform film holes

The first study evaluated the impact of introducing additional film holes through the platform. As observed in Figure 6.012 a large temperature reduction is achieved locally around the holes, (attributable to the bore cooling effects of the hole), but a temperature reduction of only about 40°F

is achieved in the trail edge fillet region. Another study evaluated the introduction of additional film holes placed in the pressure side root of the airfoil as shown in Figure 6.013.

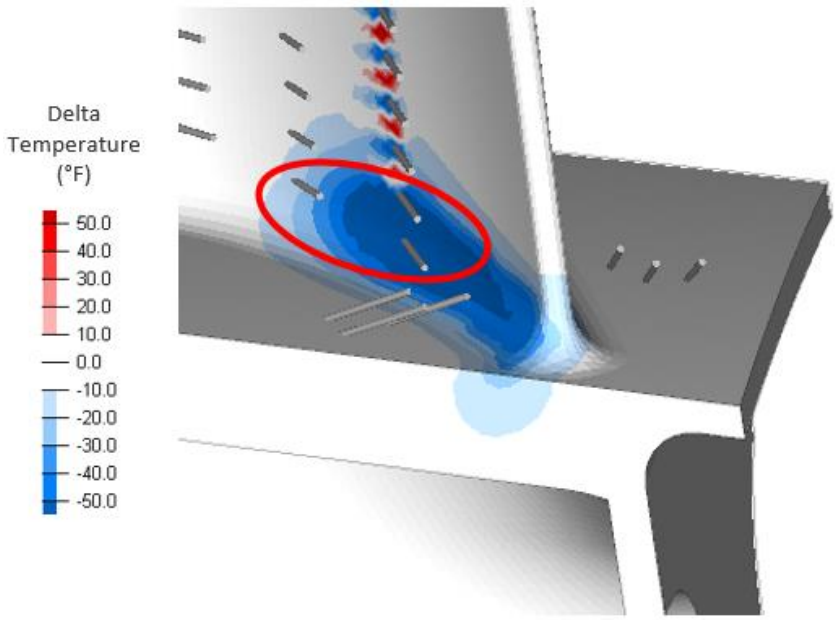

Figure 6.013: Contour plot of temperature change generated by introducing additional pressure side airfoil film holes

The additional pressure side film holes also have a limited impact at the trail edge root fillet. Given the limited availability to achieve a thermal solution to reduce temperature, mechanical solutions such as recontouring the airfoil fillet, additional trail edge thickness or a redesign of the airfoil would be recommended for future design efforts.

6.3.3.2 Shank Fillet Locations

The high strains observed at the shank fillet are driven primarily by the high inertial loading present in the high-pressure turbine due to the higher rotation speeds when compared to a low-pressure turbine. Another contributing factor is the area reduction required to pass cooling holes from the bottom of the blade, through the dovetail pressure plane and up the shank into the airfoil. Strategies to improve the stress state in this region would focus on either improving the cross-sectional area, dropping net section stresses and/or optimizing the geometry of the shank transition to the airfoil.

One design approach would be to increase the cross-sectional area of the blade, which could result in a substantial reduction of stress, but would adversely affect interfaces with other hardware or the configuration of the turbine. The primary design parameters available to manipulate the cross-sectional area are: minimize cooling passage width, increasing the shank width, and increase dovetail attachment axial length. Minimizing the width of the cooling passages would be the most difficult design option to implement. Since this cooling architecture has a wrapped internal cavity, there are limitations on the minimum radius of curvature that can be implemented without

introducing fiber damage during manufacturing. Reducing the cavity width would also make the transition to the airfoil passage geometry more challenging to manufacture. Increasing the width of the shank is a viable option, but the impact to the design of the disk and the disk posts would need to be evaluated. As the current design directly leveraged the configuration of an existing high-pressure turbine blade the blade count was fixed and the ability to increase the shank min-neck dimension was limited, even with consideration of the reduced inertial load of a CMC blade versus a blade constructed from a nickel-based alloy. One option for a new design (non-derivative) would be to consider a high-pressure turbine with a lower solidity, reducing the blade count. This design change would permit additional design space at the rim of the disk to package a larger dovetail. The last option would involve increasing the axial length of the dovetail attachment. This approach minimizes the impact to the disk attachment features, but complicates integration with the rest of the turbine architecture, primarily by moving sealing interfaces with the neighboring stator hardware. At the extreme, extending the axial length of the blade may result in additional axial length of the turbine module, which would result in additional mass added to the engine and a negative impact to the engine's specific fuel consumption.

A second design approach involves optimization of the shank geometry to minimize stress concentration factors on the blade. A key parameter attributing to the stress state of the shank fillet region is the local radius of the underlying laminate forming the surface of the shank. Figure 6.014 indicates the radius of the underlying laminate's minimum radius of the baseline cooled blade test article design.

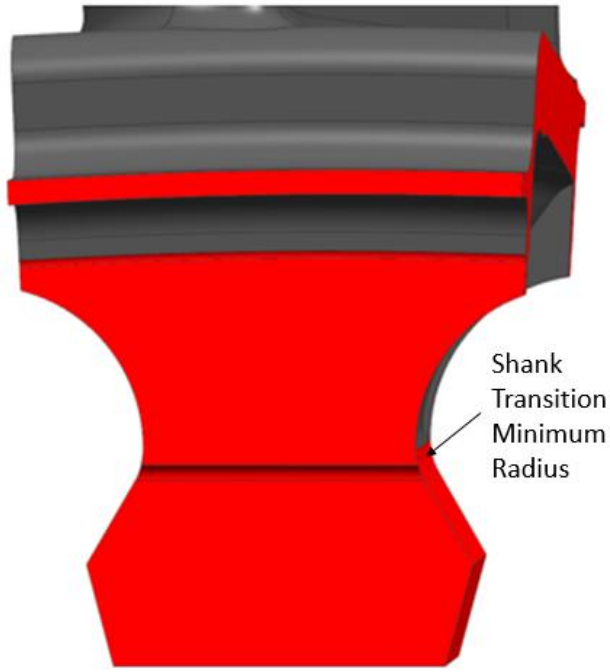

Figure 6.014: Minimum radius and location of dovetail-shank transition

By increasing this transition radius, the high strain at the shank fillet would redistribute to the broader shank region. Figure 6.015 depicts a possible redesign where the shank fillet radius could be increased to accommodate a larger fillet radius with a lower stress concentration.

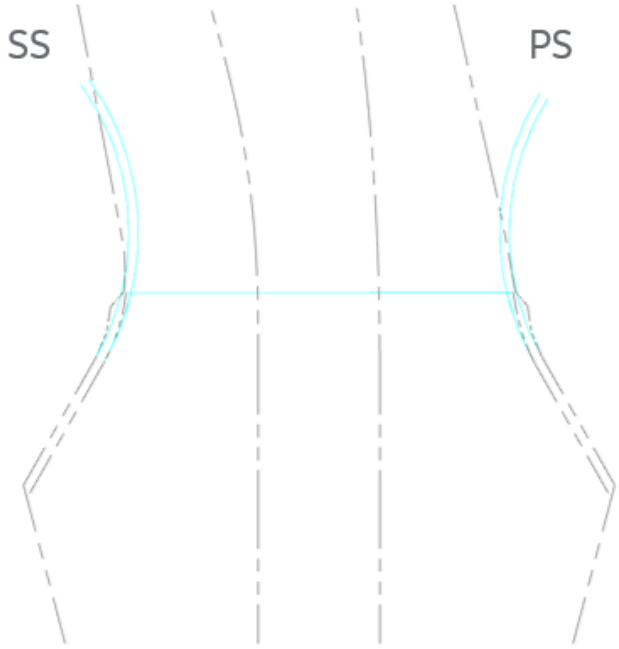

Figure 6.015: Shank fillet transition update. Original geometry shown in a dashed line with new geometry overlayed as a solid cyan line.

Updating the shank fillet to a larger radius would positively impact the strain locally at the limiting location at the shank fillet, but would have a negative impact on shank cross-sectional area, and the transition geometry of the internal cooling passages. The increase of the shank fillet results in a cross-sectional area decrease of approximately 6.5%. If implemented with a redesign of the airfoil and cooling passage geometry, some of the previously mentioned geometric challenges could be abated. This specific redesign strategy is expected be effective on the suction side of the blade where a surface curvature plot in Figure 6.016 shows a local region of high curvature.

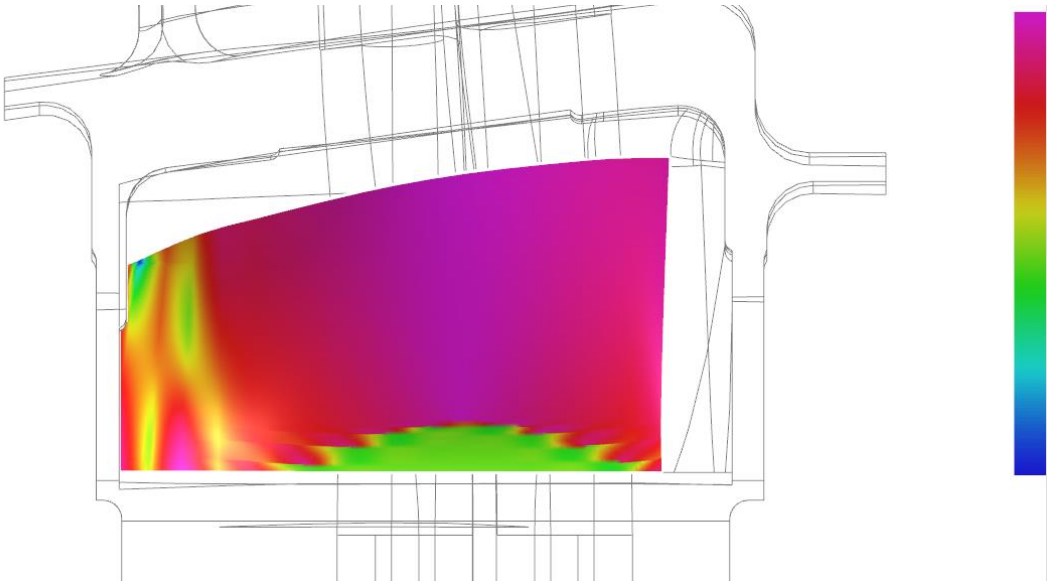

Figure 6.016: Contour plot of suction side shank surface curvature, where green-blue indicate regions of high curvature.

The area of high curvature on the lower portion of the suction side shank face is driven by the transition of the internal cavities through the shank to the root of the airfoil. Delaying or re-contouring the cooling passage geometry would mitigate the abrupt change in curvature and the stress concentration present. Several abatements are available to address the shortfall of the initial concept design, a summary table of items discussed is available in Table 6.001

Table 6.001 Design Abatement Summary

Abatement	Impact	Challenges
Additional platform cooling	Reduction in temperatures of 40°F at the trail edge root location	Increased cooling flow
Additional pressure side film cooling	Reduction in temperatures of 15°F at the trail edge root location	Increased cooling flow
Modified airfoil surface / airfoil stack	Redistribute mechanical strain away from trail edge	New aero design
Increase dovetail axial length	Lower net section stresses	Challenge with interfaces and impact to turbine length
Lower solidity airfoil design	Reduced blade count, more rim/attachment design space	Possible increased blade loading / airfoil transition challenges
Shank fillet radius increase	Decrease stress concentration locally in dovetail	Possible decrease in shank cross-sectional area
Shank face re-contour	Reduction in local stress concentration	Possible complication with laminate architecture, onion skinning

6.3.4 Analysis Conclusion

While the initial baseline design configuration of the cooled CMC blade test article has notable shortfalls relative to meeting design requirements, there are many actionable abatements that could be incorporated in a follow-on redesign of the blade architecture. When considering design derivatives of the cooled blade architecture not limited to a drop-in replacement the learnings developed from this exercise can serve as guideline for parameter optimization for cooled CMC blade architectures.

7.0 Conclusion

1. The CMC Turbine Blade Durability program successfully established a baseline design for a cooled CMC HPT blade with all the required features for operation in engine relevant conditions and advanced the state of the art in cooled CMC turbine blade design.

2. The manufacturing effort supporting the test article fabrication successfully developed tooling and manufacturing methodologies for manufacturing CMC dovetails with integrated cooling features.

3. The experimental testing programs developed learnings around the durability impact of cooling holes present in stress fields, in addition to the first fundamental understanding of damage propagation in a cooled CMC dovetail architecture.

4. The analysis task highlighted the modeling rigor required to adequately capture the stress state in sensitive design locations and understand the fundamental design drivers in a cooled CMC blade architecture as well as corrective actions and abatements to improve the design.

8.0 Symbols and Nomenclature

CMC – Ceramic Matrix Composite

DIC – Digital Image Correlation

EDM – Electrostatic Discharge Machining

eSPLCF – Strain Controlled Sustained Peak Low Cycle Fatigue

HCF – High Cycle Fatigue

HPT – High Pressure Turbine

SiC – Silicon Carbide

SPLCF – Sustained Peak Low Cycle Fatigue

9.0 Acknowledgements

The following individuals are GE Aerospace, GE Global Research, and NASA Glenn Research Center personnel who made significant contributions to the program and allowed for the successful execution and completion of the task objectives.

Task 1 Contributors:

Dane Dale (GEA), Laura Dombrowski (GEA), Cameron Farley (GEA), Zach Miller (GEA), Adam Aresty (GEA), Brian Agnew (GEA) Abby Moe (GEA), Brian Keith (GEA), Brian Corsetti (GEA), and John Calhoun (GEA)

Task 2 Contributors:

Dane Dale (GEA), Alex Ruschau (GEA), Greg Phelps (GEA), Paul Wilkerson (GEA), Betty Delaney (GEA), Matt Hockemeyer (GE GRC), and Nolan Cousineau (GEA)

Task 3 Contributors:

Dane Dale (GEA), Laura Dombrowski (GEA), Roger Seither (GEA), Kipyung Ahn (GEA), Craig Smith (NASA GRC), James D. Kiser (NASA GRC), Amjad Almansour (NASA GRC), Michael Presby (NASA GRC), Kang Lee (NASA GRC), Raymond Robinson (NASA GRC), Joe Grady (NASA GRC – Retired), Sreeramesh Kalluri (HX5, LLC), and Ramakrishna Bhatt (HX5, LLC)

Task 4 Contributors:

Dane Dale (GEA), Ashley Grooms (GEA), Ramesh Gambheera (GEA), Joel Johnston (GE GRC), Alireza Namazifard (GE GRC), Dalong Li (GE GRC), Changjie Sun (GE GRC)

10.0 References

1. Steibel, J.: Ceramic Matrix Composites Taking Flight at GE Aviation. American Ceramic Society Bulletin, vol. 98, no. 3, 2019, pp. 30–33.
2. Kalluri, S., Smith, C., Kiser J. & Almansour A. (2023). 'High-Cycle Fatigue Behavior of a SiC/SiC CMC without and with Simulated Cooling Holes', *46th Annual Conference on Composites, Materials, and Structures (CMS23)* St. Augustine, Florida; January 23-26.